Journal of Mathematical Biology (2025) 91:14
https://doi.org/10.1007/s00285-025-02245-6

A model for contractile stress fibers embedded in bulk actomyosin networks

Mariya Savinov[1] · **Charles S. Peskin**[1] · **Alex Mogilner**[1,2]

Received: 3 September 2024 / Revised: 15 April 2025 / Accepted: 5 June 2025

Abstract
Contractile cytoskeletal structures such as fine actomyosin meshworks and stress fibers are essential force-generators for mechanical phenomena in live cells, including motility, morphogenesis, and mechanosensing. While there have been many studies on the rheology and assembly of individual stress fibers, few mathematical models have explicitly modeled the bulk actomyosin network in which stress fibers are embedded, particularly not in the case of high actin turnover. Generally the extent of the interplay between embedded stress fibers and contractile bulk networks is still not well understood. To address this gap, we design a model of stress fibers embedded in bulk actomyosin networks which utilizes the immersed boundary method, allowing one to consider various stress fiber rheologies in the context of an approximately viscous, compressible, contractile bulk network. We characterize the dynamics of bulk actomyosin networks with and without embedded stress fibers, and simulate a laser ablation experiment to demonstrate the effective long-range interactions between stress fibers as well as how perturbations of stress fibers can result in symmetry breaking of the bulk actomyosin network. This paper is a part of the Special Collection "Problems, Progress and Perspectives in Mathematical and Computational Biology".

Keywords Cytoskeleton · Actomyosin · Immersed boundary method · Mechanical modeling · Fluid–structure interaction

✉ Mariya Savinov
mas10009@nyu.edu

Charles S. Peskin
peskin@cims.nyu.edu

Alex Mogilner
mogilner@cims.nyu.edu

[1] Courant Institute of Mathematical Sciences, New York University, New York, USA

[2] Department of Biology, New York University, New York, USA

Published online: 26 June 2025

Mathematical Classification 92-10 Mathematical modeling or simulation for problems pertaining to biology · 92C05 Biophysics · 92-08 Computational methods for problems pertaining to biology

1 Introduction

Essential cellular processes such as motility, morphogenesis, and mechanosensing, among others, depend on the action of force-generating subcellular structures (Ruppel et al. 2023). Composed of actin, myosin motor proteins, and other complementary components, these structures include the cytokinetic ring in cell division (Vavylonis et al. 2008), lamellipodia in motile cells (Cramer 1999), and stress fibers (SF) (Lehtimäki et al. 2021). SFs are composed of bundles of cross-linked actin filaments (Cramer et al. 1997), spanning up to tens of microns in length (Livne and Geiger 2016) with variable widths from less than 0.5 μm (Livne and Geiger 2016) to potentially up to 1 μm (Buenaventura et al. 2024), typically thick and stable in non-motile cells while thinner and more dynamic in highly motile ones (Tojkander et al. 2012). There are various classifications of SFs, particularly in the context of motile cells, outlined in reviews such as Pellegrin and Mellor (2007); Tojkander et al. (2012); Kassianidou et al. (2017). Many types of SFs are contractile (Isenberg et al. 1976; Kreis and Birchmeier 1980), containing myosin motor proteins, which convert ATP chemical energy to mechanical energy, generating forces and movement of actin filaments ultimately leading to a contractile tension along the length of the fiber. SFs additionally often have focal adhesions at their ends, connecting them to the extracellular environment. The contractile tension and adhesions of SFs are harnessed by the cell for a number of functions, such as regulation of nuclear shape (Khatau et al. 2009), persistent lamellipodial migration (Rid et al. 2005), resistance to shear in endothelial cells (Sato and Ohashi 2005), and mechanosensing (Hayakawa et al. 2008; Colombelli et al. 2009; Trichet et al. 2012).

There have been many studies on the rheology and assembly of individual SFs, both experimental (Cramer et al. 1997; Bershadsky et al. 2006; Hotulainen and Lappalainen 2006; Kumar et al. 2006; Lu et al. 2008; Russell et al. 2009; Tanner et al. 2010; Tojkander et al. 2011; Lee et al. 2018) and computational (Stachowiak and O'Shaughnessy 2009; Russell et al. 2009; Besser et al. 2011; Chapin et al. 2014; Fogelson and Mogilner 2018). The response of individual SFs to laser ablation is well characterized to be viscoelastic (Kumar et al. 2006; Tanner et al. 2010; Besser et al. 2011; Lee et al. 2018), and many have studied the dynamics by modeling SFs as active, Kelvin-Voigt-like structures (Besser et al. 2011; Chapin et al. 2014; Kassianidou et al. 2017; Bernal et al. 2022). Few mathematical models of SFs explicitly model the surrounding cytoskeleton and cytoplasm in which SFs are immersed, assuming that they contribute an external drag force, or to the internal fiber viscosity in a way which is homogeneous along the length of the fiber and independent of positioning in the cell. Dynamics relating to SF bending resistance are generally neglected, with models focusing instead on length-contraction dynamics.

However, experiments have shown that SFs are connected to and influenced by the bulk actomyosin network in cells (Vignaud et al. 2021; Riedel et al. 2024), as

well as other SFs (Kassianidou et al. 2017). For example, Vignaud et al. (2021) captured the dynamics of ablated SFs in micropatterned cells by modeling them as contractile, elastic structures embedded in an elastic and percolated cortical network. Recently, Riedel et al. (2024) computationally modeled SFs embedded in an elastic bulk medium to explain SF positioning and its relation to cellular mechanical stress. These bulk actomyosin networks are also force-generating higher-order actin structures, where myosins produce contractile forces which cells harness for essential processes such as motility (Blanchoin et al. 2014) and morphogenesis (Heisenberg and Bellaïche 2013). At the micron scale, these networks are composed of semiflexible actin filaments which interact with each other through both proteins and hydrodynamic interactions. It is well understood that these collective micron-scale interactions in percolated actin networks result in viscoelastic dynamics at the scale of tens of microns, elastic on short timescales and viscous on long timescales (Schmoller et al. 2009; Maxian et al. 2021, 2022). The high turnover rates of in vivo actomyosin networks (Brieher 2013) can make these networks effectively viscous on the timescale of minutes (Malik-Garbi et al. 2019).

The extent to which embedding SFs in active, bulk actomyosin networks impacts cell mechanics is still not well understood. Moreover, how SF dynamics in, e.g., laser ablation experiments are affected by embedding in bulk actomyosin networks has not yet been studied through mathematical modeling. To address this gap, we design a model of SFs embedded in bulk actomyosin networks which utilizes the immersed boundary method (IBM) (Peskin 1972, 2002). The IBM has been used to study fluid–structure interactions in a variety of biological contexts, such as swimming (Fauci and Peskin 1988; Tytell et al. 2010; Hamlet et al. 2011; Park et al. 2019), biofilms (Dillon et al. 1996), bleb formation (Strychalski and Guy 2013), and cell migration (Strychalski et al. 2015; Lee et al. 2017). As a computational method, the IBM is advantageous in contexts where one seeks to consider various immersed boundary rheologies. In our utilization of the IBM, the immersed boundaries are SFs and the “fluid" is the bulk actomyosin network. Though it is possible to model these networks on the microscopic level (Vavylonis et al. 2008; Maxian et al. 2021; Rutkowski and Vavylonis 2021; Maxian et al. 2022; Yan et al. 2022), discretely and stochastically, such approaches are computationally intractable at the scale of tens of microns. Continuum models have been widely used to study the dynamics of bulk actomyosin networks (Lewis et al. 2014; Linsmeier et al. 2016; Malik-Garbi et al. 2019; Le Goff et al. 2020). So, we model the network as a compressible viscous fluid, matching experimental observations in cases of the high turnover characteristic of cells (Brieher 2013; Malik-Garbi et al. 2019). Myosin motors bind and unbind from the network, advecting or diffusing depending on their respective state. We present our model for SFs as 1D viscoelastic contractile structures, and use an immersed boundary approach to couple SFs to the bulk actomyosin network. Finally, we present results for dynamics of the bulk actomyosin network with and without embedded SFs in 2D, to characterize the behaviors and inform future parameter choices and applications in 3D. Our model highlights the interplay and balance between SFs and a contractile bulk actomyosin network, and the effective hydrodynamic interactions between different SFs across cellular-scale domains. We also show that laser ablation

of SFs embedded in contractile bulk networks with fast turnover can yield a symmetry breaking effect.

2 Bulk actomyosin network model

In Fig. 1a, we show an illustration of our system of a bulk actomyosin network with embedded SFs. We model the bulk actomyosin network as a viscous, compressible fluid with velocity $\boldsymbol{u}(\boldsymbol{x})$ which is driven by active compressive stresses due to a myosin density $m(\boldsymbol{x})$. The stress tensor takes the form

$$\boldsymbol{\sigma} = [M\, m + (\lambda - 2\mu/3)\, \nabla \cdot \boldsymbol{u}]\, \boldsymbol{I} + \mu \left(\nabla \boldsymbol{u} + \nabla \boldsymbol{u}^T\right) \ . \tag{1}$$

Here, stress due to myosin is isotropic, like a negative pressure on the fluid. The constants μ and λ are the viscosity and expansion viscosity of the fluid, and M is effectively the strength of myosin contraction. The expansion viscosity λ must by positive by the second law of thermodynamics; for dilute monatomic gases, it is identically zero, but for water $\lambda \approx 3\mu$(Cramer 2012). Regardless, generally, the effect on the

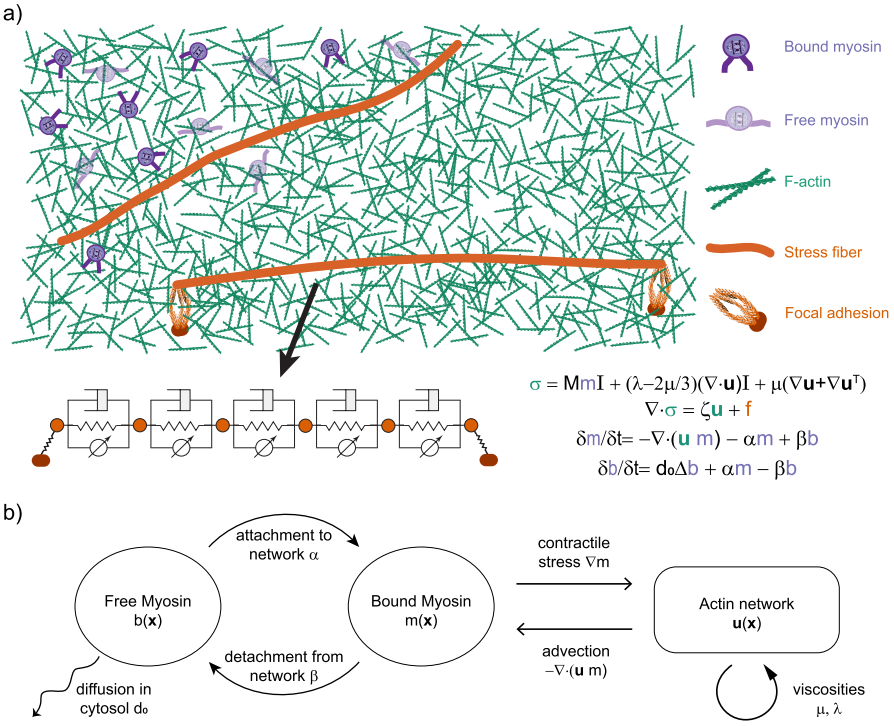

Fig. 1 **a** An illustration of the bulk actin network (green F-actin filaments), bound and free myosins (purple), embedded SFs (orange), and possible focal adhesions (orange). The contractile Kelvin-Voigt model for SFs is shown, as well as the bulk actomyosin force balance, reaction-advection, and reaction-diffusion equations. **b** A schematic of how the bound myosin, free myosin, and actin network interact with one another

flow of the expansion viscosity term in (1) tends to be small, but has been shown to be substantial in extreme cases such as when $\lambda \gg \mu$ in large Reynolds number flow (Cramer and Bahmani 2014).

At the cellular scale, the Reynolds number is small, close to 10^{-5}(Mogilner and Manhart 2018), so there is effectively no inertia (Malik-Garbi et al. 2019). Thus the network evolves by a balance of internal forces, defined by stress $\boldsymbol{\sigma}$ in (1), with external forces. We assume, following previous models (Rubinstein et al. 2009), that the network is subject to drag forces $\zeta \boldsymbol{u}$ with the environment (in this case the cytosol and/or underlying surface) and forces $\boldsymbol{f}$ from any immersed boundaries (in our case, SFs). This yields a governing equation

$$\begin{aligned} \nabla \cdot \boldsymbol{\sigma} &= \boldsymbol{f}_{\text{external}} \,, \\ \underbrace{M \nabla m}_{\text{myosin}} + \underbrace{(\lambda + \mu/3) \nabla (\nabla \cdot \boldsymbol{u}) + \mu \Delta \boldsymbol{u}}_{\text{viscosity}} &= \underbrace{\zeta \boldsymbol{u}}_{\text{drag}} + \underbrace{\boldsymbol{f}}_{\text{fiber}} \,. \end{aligned} \tag{2}$$

Throughout the paper, we assume that the actin network occupies a simply connected domain Ω, in which (2) applies. Often, the boundaries of such networks are free, but we will consider an equally ubiquitous case of a fixed domain where the high turnover of the network means the network quickly reassembles at the boundary to keep the domain fixed. We will assume, again following many previous models, that a no-stress boundary condition holds on this domain boundary:

$$\boldsymbol{\sigma} \cdot \hat{\boldsymbol{n}} = \boldsymbol{0} \quad \text{on the boundary } \partial\Omega \,. \tag{3}$$

Note that we do not consider a mass-conservation equation for the actin network itself, which would be an advection-reaction equation such as $\partial\rho/\partial t = -\nabla \cdot (\boldsymbol{u}\rho) - \delta_d \rho + \delta_a$, where the sample reaction terms represent disassembly (with rate δ_d) and assembly (with rate δ_a) of the actin network. Generally, the viscosities μ and λ may then depend on the density ρ of the actin network, with denser networks being more viscous. However, as we are considering in vivo dynamics, turnover of actin is generally fast and the reaction terms dominate over advection, eliminating variances in the apparent viscosity. For this reason, we do not consider a mass-conservation equation for the actin network.

In (2), the myosin density $m(\boldsymbol{x})$ represents the fraction of myosin which is bound to and advected by the network. However, myosin attachment to actin is dynamic, as myosin motors attach and detach stochastically at the molecular level. At the continuum level, this is reflected in there being two myosin populations in bulk: bound myosin m and free myosin b, which we assume exchange with rates α and β(Rubinstein et al. 2009). While the bound myosin is advected by the network, we assume that the free myosin effectively freely diffuses in the cytosol. Thus, we model these two population dynamics by coupled reaction-advection and reaction-diffusion equations:

$$\begin{aligned} \frac{\partial m}{\partial t} &= -\nabla \cdot (\boldsymbol{u} m) - \alpha\, m + \beta\, b \ , \\ \frac{\partial b}{\partial t} &= d_0\, \Delta b + \alpha\, m - \beta\, b \ . \end{aligned} \tag{4}$$

Here, d_0 is the diffusion coefficient for the free myosin, α is the detachment rate, and β is the attachment rate. We assume effectively no-flux boundary conditions on the two myosin populations:

$$\begin{aligned} m &= 0, \quad \boldsymbol{x} \in \partial\Omega \quad \text{if} \quad \boldsymbol{u} \cdot \boldsymbol{n} < 0 \ , \\ \frac{\partial b}{\partial n} &= 0, \quad \boldsymbol{x} \in \partial\Omega \ . \end{aligned} \tag{5}$$

Here, $\boldsymbol{n}$ is the outward facing normal of Ω. The first part of (5) describes an inflow boundary condition on the bound myosin m which enforces that no myosin flows into the domain Ω. Note that there is no outflow condition because myosin generates contractile stresses and, in simulations with nonzero myosin densities, the network flow velocity is always directed inward.

The myosin dynamics Eqs. (4) together with the force balance (2) and boundary conditions (3) and (5) effectively model the behavior of a bulk actomyosin network. Figure 1b shows a schematic of the action of the various parameters and components of the bulk network. In simulations, we will consider a fixed 2D rectangular domain Ω.

2.1 Scaling and non-dimensionalization

Given a spatial scale R (domain size) and myosin density scale m_0, we non-dimensionalize the actomyosin variables by

$$\boldsymbol{x} \to R\boldsymbol{x}\,, \quad \boldsymbol{u} \to \left(\frac{M m_0}{\zeta R}\right)\boldsymbol{u}\,, \quad m \to m_0\, m\,, \quad b \to m_0\, b\,, \quad \text{and} \quad \boldsymbol{f} \to M m_0 R \boldsymbol{f}\ .$$

This then yields the fully nondimensional force-balance equation

$$\nabla m + (\lambda + \mu/3)\, \nabla\, (\nabla \cdot \boldsymbol{u}) + \mu \Delta \boldsymbol{u} = \boldsymbol{u} + \boldsymbol{f} \tag{6}$$

with two non-dimensional viscosity constants μ and λ which relate to their dimensional counterparts by

$$\frac{\mu}{\zeta R^2} \to \mu \quad \text{and} \quad \frac{\lambda}{\zeta R^2} \to \lambda\ .$$

There is a very useful notion of hydrodynamic length ℓ_0, which relates to viscosity and drag by $\ell_0 = \sqrt{\mu/\zeta}$, that shows how far in space a concentrated force spreads (Rubinstein et al. 2009). The nondimensional viscosity coefficient μ in (6) is identical to the ratio of the hydrodynamic length to the domain size squared: $\mu = (\ell_0/R)^2$. If

μ is large, then the hydrodynamic length is large relative to the domain size, and vice versa if μ is small.

Meanwhile, the myosin density equations nondimensionalize to the same form as (4). The three non-dimensional parameters relate to their dimensional counterparts by

$$\frac{\zeta R^2}{M m_0}\alpha \to \alpha\,, \quad \frac{\zeta R^2}{M m_0}\beta \to \beta\,, \quad \text{and} \quad \frac{\zeta}{M m_0} d_0 \to d_0\,,$$

where the left-side is in dimensions. Note that $\zeta R^2/M m_0$ is the characteristic timescale determined by the time of contraction driven by the balance of myosin-generated forces and effective external drag.

3 Stress fiber model

Consider the SF as a 1D structure defined by Lagrangian points $\boldsymbol{X}(q)$, where $q \in \Gamma$ denotes the position along the fiber Γ. There is a net internal force $\boldsymbol{F}(q)$ along the length of the fiber. At low Reynolds number, the internal force is equal and opposite to the external force on the fiber from the network, which in turn is equal and opposite to the force on the network from the fiber:

$$\boldsymbol{F} = -\boldsymbol{F}_{\text{external}} = -\boldsymbol{F}_{\text{force on fiber from network}} = \boldsymbol{F}_{\text{force on network from fiber}}\,.$$

This allows us to take advantage of an immersed boundary perspective, which typically relies on the immersed boundary being mass-less: the additional force $\boldsymbol{f}$ we see in (2) is related to the internal force $\boldsymbol{F}(q)$ in the fiber by

$$\boldsymbol{f}(\boldsymbol{x}, t) = \int \boldsymbol{F}(q)\, \delta\left(\boldsymbol{x} - \boldsymbol{X}(q, t)\right)\, dq\,. \tag{7}$$

Given information as to the configuration of the fiber, one can solve just the bulk network Eq. (2), as opposed to two coupled equations for the network and fiber independently. We assume a no-slip boundary condition, as opposed to considering a formulation where the fibers move according to a slip velocity and contribution from the background bulk actomyosin network flow, such as Kumar and Graham (2015) do for blood flow or Saintillan et al. (2015) for active particles. Our choice is motivated by previous experimental and modeling studies, which have shown that SFs are connected to and embedded in the bulk actomyosin network in cells (Vignaud et al. 2021; Riedel et al. 2024). Considering that SFs and the bulk networks are composed of the same building blocks, it is likely they may even interact directly through their complementary proteins, making a no slip boundary condition potentially even more relevant. So, the SF (the immersed boundary) moves with the fluid velocity $\boldsymbol{u}(\boldsymbol{x}, t)$:

$$\frac{\partial \boldsymbol{X}}{\partial t}(q, t) = \int_{\Omega} \boldsymbol{u}(\boldsymbol{x}, t)\, \delta\left(\boldsymbol{x} - \boldsymbol{X}(q, t)\right)\, d\boldsymbol{x}\,. \tag{8}$$

We will consider five classes of forces along the fiber: elastic forces $\boldsymbol{F}^e$ due to fiber resistance to stretch/compression, bending forces $\boldsymbol{F}^b$ due to fiber resistance to bending, viscous forces $\boldsymbol{F}^v$ due to fluid-like fiber behaviors, myosin forces $\boldsymbol{F}^m$ due to myosin activity, and finally adhesion forces $\boldsymbol{F}^a$ due to adhesions at the SF ends. In all,

$$\boldsymbol{F}(q) = \boldsymbol{F}^e(q) + \boldsymbol{F}^b(q) + \boldsymbol{F}^v(q) + \boldsymbol{F}^m(q) + \boldsymbol{F}^a(q) \ .$$

A schematic of the model can be seen in Fig. 1a, with the exception of the bending resistance response. We nondimensionalize the fiber forces, described following, using the same scales introduced in Sect. 2.1 (for nondimensionalization details, see Supplement Sect. 1). The entire system's parameters, dimensional values, and nondimensional counterparts are listed in Table S2 in the Supplement.

3.1 Elastic forces

Consider an elastic fiber with rest length L_0. It has some continuous elastic energy due to stretch or compression given by

$$E_e\left[\boldsymbol{X}(q)\right] = \int_0^{L_0} \frac{K_E}{2} \left(\left\| \frac{\partial \boldsymbol{X}}{\partial q} \right\| - 1 \right)^2 dq \ . \tag{9}$$

The tension associated with this energy is

$$T = K_E \left(\left\| \frac{\partial \boldsymbol{X}}{\partial q} \right\| - 1 \right) \tag{10}$$

which is in the direction $\boldsymbol{\tau}$, the unit tangent vector:

$$\boldsymbol{\tau} = \frac{\partial \boldsymbol{X}/\partial q}{\|\partial \boldsymbol{X}/\partial q\|} \ . \tag{11}$$

The elastic force density on the fiber is then given by the negative of the variational derivative of the energy functional (9), as outlined in (Peskin 2002), yielding

$$\boldsymbol{F}^e(q) = -\frac{\delta E_e}{\delta \boldsymbol{X}} = \frac{\partial}{\partial q}\left(T\boldsymbol{\tau}\right) \ . \tag{12}$$

Note that the elastic energy of the fiber is in terms of the parameter K_E with units of force, unlike a traditional spring constant, which has units of force over length. K_E is essentially the Young's modulus of the fiber (see Appendix A for details).

3.2 Bending forces

Suppose the fiber has bending resistance, meaning that curvature has an associated energy given by

$$E_b\left[\boldsymbol{X}(q)\right] = \int_0^{L_0} \frac{K_B}{2} \left\| \frac{\partial^2 \boldsymbol{X}}{\partial q^2} \right\|^2 dq \ . \tag{13}$$

The elastic force density on the fiber is then

$$\boldsymbol{F}^b(q) = -\frac{\delta E_b}{\delta \boldsymbol{X}} = -K_B \frac{\partial^4 \boldsymbol{X}}{\partial q^4} \ . \tag{14}$$

This variational derivative (14) of the bending energy is a fourth derivative of the configuration $\boldsymbol{X}$(i.e. a second derivative of the curvature), so this component of the system is particularly stiff in the context of numerically solving for the fiber dynamics.

3.3 Viscous forces

It was shown that SFs exhibit viscoelastic behavior (Kumar et al. 2006; Tanner et al. 2010; Besser et al. 2011; Lee et al. 2018). The nature of this viscoelasticity, however, depends on context and varies between systems. Previous research has shown that fibers in vitro behave like Kelvin-Voigt solids, which are elastic on long timescales but resistant to fast deformation (Kumar et al. 2006; Stachowiak and O'Shaughnessy 2009). Such materials are schematically represented as a spring and viscous element in parallel, with a Young's modulus Y and viscosity η. Supposing a 1D fiber with rest length L_0 is stretched to length L, the strain $\varepsilon(t) = (L - L_0)/L_0$ yields stress

$$\sigma(t) = \eta \frac{d\varepsilon}{dt} + Y\,\varepsilon(t) = \frac{\eta}{L_0}\frac{dL}{dt} + Y\left(\frac{L}{L_0} - 1\right) \ .$$

For fiber cross-sectional area A, the corresponding force is

$$F = A\sigma = \frac{\eta\, A}{L_0}\frac{dL}{dt} + \frac{Y A}{L_0}L = \frac{\xi}{L_0}\frac{dL}{dt} + K_E\left(\frac{L}{L_0} - 1\right) \ .$$

Notice the second term is tension (10), but for the case of a single spring. The first term is the viscous force determined by deformation rate, with viscous coefficient $\xi = \eta A$. The viscous force on the fiber, in our coordinate system, is then given as

$$\boldsymbol{F}^v = \xi \frac{\partial}{\partial t}\left\| \frac{\partial \boldsymbol{X}}{\partial q} \right\| \boldsymbol{\tau} \tag{15}$$

where the tangent vector (11) defines the direction of the force.

3.4 Myosin forces

Many stress fibers, such as transverse arcs and ventral fibers (Tojkander et al. 2012), are contractile due to the action of myosin motor proteins. To incorporate contractility, we follow the approach of previous SF models (Kaunas et al. 2010; Besser et al.

2011; Kassianidou et al. 2017) which consider a linearized force-velocity relation for the myosin-generated contractile force. This relation is written as

$$F^m = F_s \left(1 + \frac{1}{v_0 L_0} \frac{dL}{dt}\right) \tag{16}$$

where F_s is the stall force and v_0 is the free velocity per unit length. Namely, if the fiber is not deforming, myosin motors generate force (tension) F_s along the SF length; if each fiber's unit contracts with free velocity, then myosin do not generate any force. This force F^m is parallel to the tangent direction $\boldsymbol{\tau}$ along the fiber given in (11).

3.5 Adhesion forces

Many SFs have focal adhesions at the ends, so as the fiber contracts it must do so under tension from these focal adhesions. Some studies have also suggested that there are adhesions to the environment throughout the length of the fiber (Sherrard et al. 2021). We can implement the effect of focal adhesions through the use of target points. Suppose we have an adhesion at a point $\boldsymbol{Z}_j$. We model adhesions as linear springs with rest length zero, serving to keep the fiber position $\boldsymbol{X}_j$ close to $\boldsymbol{Z}_j$, the site of the adhesion. The corresponding force of this adhesion is then simply

$$\boldsymbol{F}_j^a = -k_{adh} \left(\boldsymbol{X}_j - \boldsymbol{Z}_j\right) \tag{17}$$

where the parameter k_{adh} is the force per unit length of the adhesive spring. However, if the adhesions are distributed uniformly along the length of the fiber, we instead consider discrete forces

$$\boldsymbol{F}_j^a = -k_{adh} \frac{\boldsymbol{X}_j - \boldsymbol{Z}_j}{\Delta q} \tag{18}$$

where Δq is the spatial distance between adhesion points $\boldsymbol{X}_j$.

4 Immersed boundary method for a fiber embedded in an actomyosin network

Consider now that the fiber is immersed in a global actin mesh, which behaves like the active compressible viscous fluid outlined in Sect. 2. Following the introduction in Sect. 3, let $\boldsymbol{F}(q)$ define the force along the fiber (and thus the force the fiber exerts on the fluid). The traditional immersed boundary method (IBM) with no-slip boundary conditions has governing Eqs. (6), (7), and (8), restated here:

$$\text{Fluid force balance:} \quad \nabla m + (\lambda + \mu/3)\nabla(\nabla \cdot \boldsymbol{u}) + \mu\Delta\boldsymbol{u} = \boldsymbol{u} + \boldsymbol{f} \ , \tag{6}$$

$$\text{Force spreading:} \quad \boldsymbol{f}(\boldsymbol{x},t) = \int \boldsymbol{F}(q)\delta(\boldsymbol{x} - \boldsymbol{X}(q,t))\, dq = \boldsymbol{S}(\boldsymbol{X})\boldsymbol{F}(q) \ , \tag{7}$$

$$\text{Fiber equation of motion:} \quad \frac{\partial \boldsymbol{X}}{\partial t}(q,t) = \int_{\Omega} \boldsymbol{u}(\boldsymbol{x},t)\,\delta(\boldsymbol{x} - \boldsymbol{X}(q,t))\, d\boldsymbol{x} = \boldsymbol{S}^*(\boldsymbol{X})\boldsymbol{u} \ . \tag{8}$$

Here we define the spreading operator $\boldsymbol{S}$, which has adjoint $\boldsymbol{S}^*$ defining the interpolation operator. The two operators must be adjoint to one another if energy conservation is required (Peskin 2002).

Previous studies have shown that immersed boundaries have some hydrodynamic radius r_h, associated with the discretized delta function which depends directly on the Eulerian grid size h (Peskin 2002; Bringley and Peskin 2008). This hydrodynamic radius is typically of $O(h)$, such as $r_h \sim 1.2h - 1.4h$ in the Stokes case (Bringley and Peskin 2008; Maxian and Peskin 2020). So, in order to resolve the diameter of the body, the Eulerian grid size h is chosen so the physical fiber radius a matches the hydrodynamic radius r_h. For some cytoskeletal components, the physical radius a can be very small, making h prohibitively small. In traditional IBM, the Eulerian and Lagrangian grid sizes need to be comparable (Peskin 2002; Bringley and Peskin 2008), so if the Eulerian grid is small, the Lagrangian discretization size must also be small for stability. Thus, the consequence of a small immersed boundary radius a is a stiff system of equations which requires a small timestep Δt to resolve the behavior.

Stress fibers have variable widths, often smaller than 0.5 μm (Livne and Geiger 2016) but could potentially be as large as a micron in width (Buenaventura et al. 2024). In this work, we will apply our IBM formulation for the case of thicker SFs (≈ 0.5 μm in diameter) in thin actomyosin bulk networks spread on cellular scales (≈ 50 μm domain sizes). The 2D problem is applicable for example to questions regarding actomyosin and SF dynamics in thin cells spread on flat surfaces (Ruppel et al. 2023). In such cases, it is sufficient to consider grid sizes $h \sim 1/200 - 1/100$ to simulate fibers of realistic thickness.

4.1 Temporal discretization

Our spatial discretization of the spreading of the fiber force to the fluid (7) and the interpolation of the fluid velocity to the fiber (8) follows previous work, where the δ-functions are approximated with the four-point delta function $\delta_{\Delta x,\Delta y}$, detailed in Appendix E.1. The force spreading (7) is discretized as

$$\boldsymbol{f}(\boldsymbol{x},t) = \sum_{k=1}^{N_b} \boldsymbol{F}_k(\boldsymbol{X}_1,\ldots,\boldsymbol{X}_{N_b})\,\delta_{\Delta x,\Delta y}(\boldsymbol{x} - \boldsymbol{X}_k(t)) \tag{19}$$

and the interpolation of the fluid velocity onto the Lagrangian grid is discretized as

$$[\boldsymbol{S}^*\boldsymbol{u}]_k = \sum_{\boldsymbol{x}} \boldsymbol{u}(\boldsymbol{x},t)\,\delta_{\Delta x,\Delta y}(\boldsymbol{x} - \boldsymbol{X}_k(t))\,\Delta x\Delta y \ . \tag{20}$$

As the Eulerian grid is finitely large and the delta function is compactly supported, the sum above is finite in both components. The spatial discretization $\boldsymbol{F}_k$ of the fiber forces $\boldsymbol{F}(q)$Appendix C is outlined in.

We solve the network force balance equation using a second-order finite difference scheme, as outlined in Appendix B, and denote the resultant discretized force balance equation as

$$(\lambda + \mu/3)\, \boldsymbol{D}\, (\boldsymbol{D} \cdot \boldsymbol{u}) + \mu L \boldsymbol{u} = -\boldsymbol{D} m + \boldsymbol{u} + \boldsymbol{f} \tag{21}$$

where $\boldsymbol{D}$ is the discretized Del operator and L is the discretized Laplacian.

In the case of a SF without velocity-dependent forces, it is straightforward to timestep, as the fiber configuration determines fiber force and thus bulk velocity, which interpolates to the fiber velocity for timestepping (see details in Appendix E.2). However, for a contractile, viscoelastic fiber, the fiber forces depend on *both* the current configuration $\boldsymbol{X}$ and fiber velocity $\boldsymbol{U}$:

$$\boldsymbol{F} = \underbrace{\boldsymbol{F}^e(\boldsymbol{X}) + \boldsymbol{F}^a(\boldsymbol{X})}_{\text{nonlinear in } \boldsymbol{X}} + \underbrace{\boldsymbol{F}^b(\boldsymbol{X})}_{\text{linear in } \boldsymbol{X}} + \underbrace{\boldsymbol{F}^v(\boldsymbol{X}, \boldsymbol{U}) + \boldsymbol{F}^m(\boldsymbol{X}, \boldsymbol{U})}_{\text{nonlinear in} \boldsymbol{X}, \text{ linear in } \boldsymbol{U}} .$$

As such, as opposed to the traditional IBM fiber equation of motion (8), we have an implicit equation for the fiber velocity $\boldsymbol{U}$:

$$\frac{\partial \boldsymbol{X}}{\partial t} = \boldsymbol{U} = \boldsymbol{S}^*(\boldsymbol{X})\, \boldsymbol{u}(\boldsymbol{X}, \boldsymbol{U}) \ . \tag{22}$$

To determine the fiber configuration over time, we need to solve (22) with an iterative approach. We choose to timestep with a fixed point iteration algorithm, where we use the previous fiber velocity $\boldsymbol{U}^{n-1}$ as an initial "guess" for the current velocity $\boldsymbol{U}^{n,(0)}$. Then, the updated fiber velocity $\boldsymbol{U}^{n,(m)}$ and configuration $\boldsymbol{X}^{n+1,(m)}$ at step m of the iteration are given by

$$\frac{\boldsymbol{X}^{n+1,(m)} - \boldsymbol{X}^n}{\Delta t} = \boldsymbol{U}^{n,(m)} = \boldsymbol{S}^*(\boldsymbol{X}^n)\, \boldsymbol{u}\left(\boldsymbol{X}^n, \boldsymbol{U}^{n,(m-1)}\right) \ . \tag{23}$$

Once the relative change in either the fiber velocity or configuration reaches some tolerance, one takes the last output of the fixed point iteration as defining the updated velocity and configuration.

In principle, one could choose to only iterate at initial time $t = 0$, and at later times take only $m = 1$ iterative steps, which would correspond to time-lagging the velocity. Such an approach was used, for example, by Strychalski and Guy (2012) to simulate Kelvin–Voigt immersed structures in Stokes flow. However, in instances where the forces change dramatically, e.g. due to tension release in laser ablation, it would be necessary to iterate longer to use a more accurate fiber velocity. In practice, we find the most expensive iterative step to be the first one, with later timesteps

requiring far fewer iterations, but implement a tolerance condition at each timestep for consistency.

We find that our implementation yields a restriction on the internal viscosity of the fiber ξ as it relates to the fluid viscosity μ. We observe that, for a fixed Eulerian grid, there is typically some critical value ξ/μ above which the initial fixed point iteration does not converge. This is similar to the restriction found by Strychalski and Guy (2012). The restriction on ξ/μ is due to additional numerical stiffness arising from spatial derivatives of the configuration velocity in the governing equations of the fiber, corresponding to the viscous resistance to deformation. In our simulations, we take the maximal value of ξ for which our method converges.

5 Results

5.1 Bulk actomyosin network dynamics

Let us consider the bulk actomyosin network without an embedded stress fiber. The network's dynamics are governed by five nondimensional parameters: the myosin detachment rate α, the myosin attachment rate β, the free myosin diffusion coefficient d_0, the first fluid viscosity μ, and the expansion fluid viscosity λ. One important feature of our model is the positive feedback between the bound myosin, which is advected by the actin network, and the actin network, which is driven by gradients in the bound myosin distribution. Consider the following scenario: suppose there is a concentration of bound myosin in a region of characteristic size $\ell < R$ somewhere in the network. Myosin forces drive network contraction, flowing inward around the region and thus causing its characteristic size to shrink. If myosin remains bound to the network, the same mass of myosin now occupies a smaller region, so there is then a larger gradient of myosin and, as a result, a larger contractile force. If not for the exchange of bound and free myosin as well as network viscous resistance to contraction, this contractile positive feedback would continue, compressing the myosin into a very small region of the domain. Fig. 1b depicts a schematic of this inherent interplay of factors.

To investigate the roles and careful balance of parameters in the actomyosin network, consider a spot of bound myosin represented by the distribution

$$m(x,y) = \exp\left(-(x-x_0)^2/0.1^2 - (y-y_0)^2/0.1^2\right) . \tag{24}$$

Consider first the impact of viscosity. Figure 2a shows the numerical solutions for actin network flows around a centered myosin spot $(x_0, y_0) = (0.5, 0.5)$ for different orders of magnitude of μ and $\lambda = 2\mu/3$[1] (see Fig. S1 for the case of a spot in the corner). From left to right in Fig. 2a, as the viscosity parameters increase the

[1] Note that we take $\lambda = 2\mu/3$ so that both viscosity terms in (6) have the same coefficient. Changing λ does not result in qualitatively different flow profiles compared with increasing μ and λ together. For details, see Fig. S2.

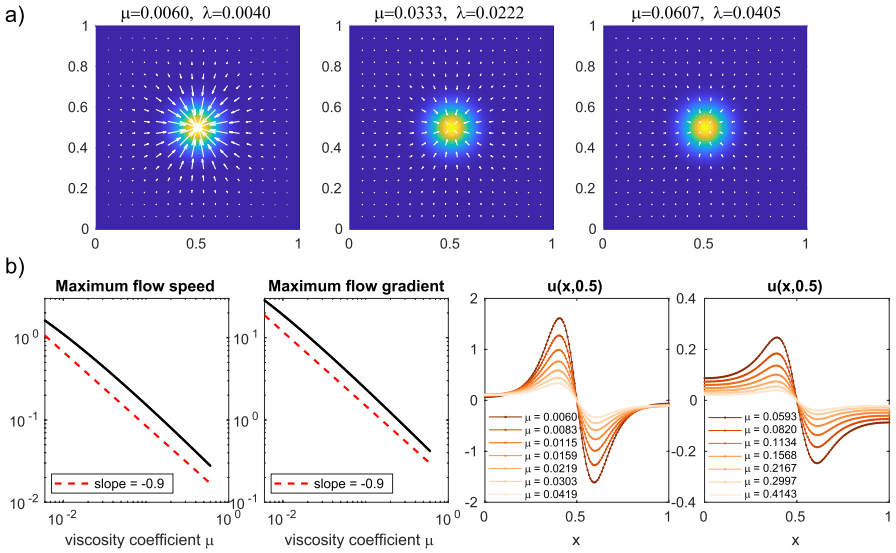

Fig. 2 **a** Numerical solutions for the actomyosin network flow for different network viscosities in the case of a gaussian-like bound myosin distribution (24) centered in a square domain $\Omega = [0, 1] \times [0, 1]$. The first viscosity coefficient μ is varied and the expansion viscosity $\lambda = 2\mu/3$ in all cases. The flow quiver arrows are identically scaled between all subplots, such that a flow speed of 1 appears as an arrow of size 0.07 in the domain. **b** Quantitative differences in flow properties around the myosin distribution in (**a**) as a function of changing actin network viscosity μ, $\lambda = 2\mu/3$. The left two columns show the maximum flow speeds and gradients, respectively, as a function of μ(log-log scale). The right two columns shows the flow distribution along the horizontal midline of the myosin peak as a function of position x for $\mu \in [0.006, 0.4143]$, with lighter colors corresponding to larger values of μ

flow speed decreases. In Fig. 2b, we see the maximum flow speed and maximum flow gradient decrease approximately like $1/\mu^{0.9}$, with a centripetal-like flow profile which decays as μ and λ are increased (dark to light). It is clear that flow speeds and gradients are most sensitive for small μ and λ. Recall that the nondimensional viscosity is proportional to the hydrodynamic length squared ($\mu = \ell_0^2/R^2$). One can interpret hydrodynamic length as follows: if ℓ_0 is large, the actin network resists flow primarily due to internal friction rather than from drag with its environment. Effectively, the network is very stiff, and effects of small shear stresses are felt at long range, integrating both the internal friction and external drag over a large size. If on the other hand ℓ_0 is small, resistance to flows is significantly more local. Thus, as μ is increasing, the effective hydrodynamic length ℓ_0 increases and the network grows stiffer, so forcing from myosin contraction is resisted at distances further and further away from the myosin spot. This explains the flow speed and gradient sensitivity to small viscosity μ.

Given such flows as in Fig. 2, the bound myosin spot would in principle start to compact, and potentially migrate if it is off-center. What sort of myosin distributions are steady depends not only on the fluid viscosities μ and λ, but also on the myosin unbinding and binding parameters α and β and the diffusion coefficient d_0. As suggested in Fig. 1, the diffusion of free myosin could act as a balance to the contraction and compaction of myosin, conditionally on the reaction rates α and β being suf-

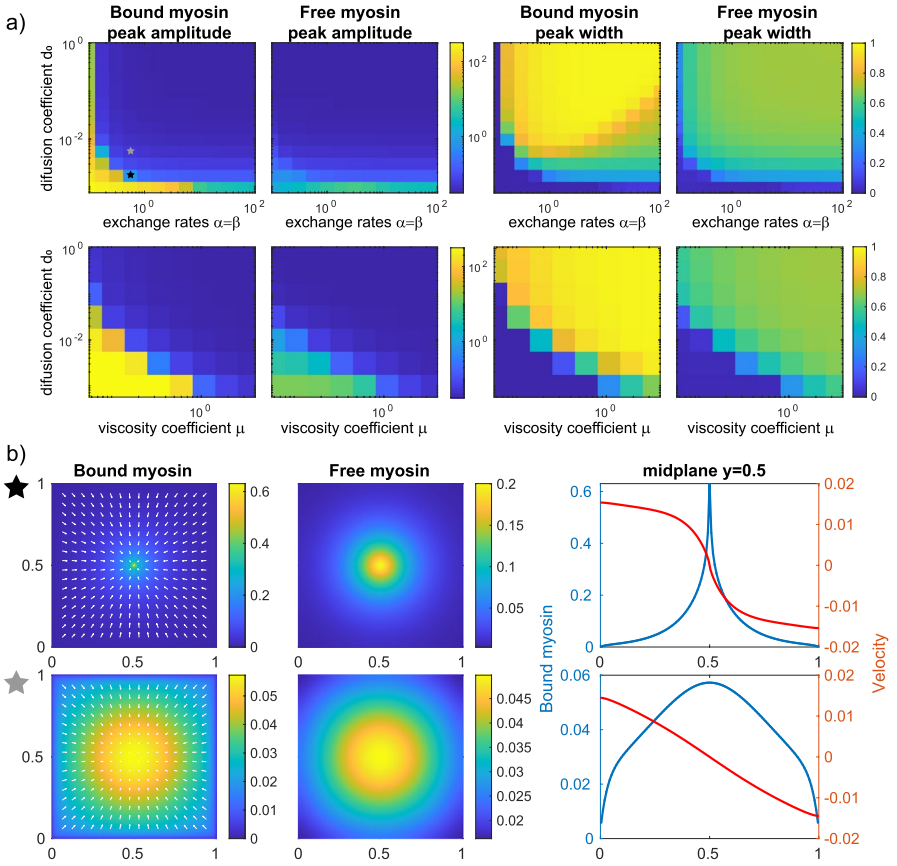

Fig. 3 **a** The peak amplitudes (left) and half-widths (right) for steady state distributions of bound and free myosin in the cases of varying the diffusion coefficient d_0 and reaction rates $\alpha = \beta$ for fixed $\mu = 0.6$, $\lambda = 0.4$(top) and varying the diffusion coefficient d_0 and viscosity coefficient μ, $\lambda = 2\mu/3$ for fixed $\alpha = \beta = 1$(bottom). The myosin populations are initialized both with distribution (24), depicted in Fig. 2a. **b** The final steady state distributions of bound and free myosin when $\alpha = \beta = 0.5623$, $\mu = 0.6$, and $\lambda = 0.4$ with $d_0 = 0.00178$(top) and $d_0 = 0.00562$(bottom)

ficiently large. However, it is unclear how large or small α, β, and d_0 should be to achieve different steady distributions.

Consider the initial condition of Fig. 2a, and fix the fluid viscosities $\mu = 0.6$ and $\lambda = 0.4$. Our aim is to assess the qualities of a 'steady state myosin spot', in terms of the bound and free myosin maximal peak values and peak widths, from an initial starting point of maximum amplitude 1 and width of approximately 0.1665. We simulate the actomyosin system for different d_0 and $\alpha = \beta$ choices[2] until the distribution of bound myosin stops changing within some tolerance. The first row of Fig. 3a shows the resulting bound and free myosin final peaks and widths. We see that even relatively small diffusion coefficients are sufficiently large to smooth out myosin dis-

[2] Note that we keep α and β equal, as we do not observe significant changes in the results when the binding and unbinding rates are of the same order of magnitude.

tributions, so long as the exchange rates are fast enough (e.g. $\alpha = \beta > 0.5$). Consider for example the two parameter sets denoted by a black star and gray star in Fig. 3a, for which the corresponding steady state distributions are shown in Fig. 3b. In the smaller diffusion coefficient case, the bound myosin distribution is sharply peaked at the center, but increasing the diffusion coefficient by roughly a factor of three results in a very smooth, nearly uniform myosin distribution. On the other hand, Fig. 3a also demonstrates that the diffusion coefficient eventually becomes irrelevant if the exchange of bound and free myosin is small, in which case the bound myosin compacts very quickly to a peak of width $\ll 1$ and it does not unbind from the network fast enough to decrease the contraction speed. A similar result occurs if $d_0 = 0.001$, where even if the exchange rates are fast, the diffusion is too slow to redistribute the myosin fast enough to prevent compaction of the spot.

Figure 3a further demonstrates that as α and β become large, the bound and free myosin characteristics start to match– in the limit of large exchange rates α and β, the exchange of bound and free myosin is the fast process of (4) while the advection and diffusion terms are relatively slow. In this limit, $m \approx \beta b/\alpha$ and the total myosin distribution $M = m + b$ obeys the modified advection–diffusion equation $\partial M/\partial t = -\beta \nabla \cdot (\boldsymbol{u} M) / (\alpha + \beta) + \alpha d_0 \Delta M / (\alpha + \beta)$. So, Fig. 3a confirms that as $\alpha = \beta$ becomes large, the myosin distributions approach $m \approx b \approx M/2$, and this limit is reached faster for smaller diffusion coefficients d_0, where the exchange rates α and β become the dominating terms more quickly.

The unbinding of myosin from the network and then diffusing outward is not the only process which balances the positive feedback of the advected myosin inducing contraction on the network. Recall Fig. 2b, which showed that as fluid viscosity increases, the maximum flow speed of the network decreases. In principle, a larger diffusion coefficient could still yield a sufficiently concentrated myosin distribution if the flow speeds were higher. Fixing $\alpha = \beta = 1$, the bottom row of Fig. 3a shows how the bound and free myosin peak amplitudes and widths change when varying viscosity μ($\lambda = 2\mu/3$) and diffusion coefficient d_0. As expected, increasing diffusion or increasing the actin network viscosity yields similar effects on the network, where the bound myosin quickly transitions from a highly concentrated distribution to a relatively smooth and uniform distribution. The effect on the free myosin is analogous. Overall, Fig. 3 shows that when it comes to myosin 'spot'-like distributions, the actomyosin network tends to the extremes of highly concentrated or highly smoothed myosin distributions, with only fine-tuned parameters achieving a balance between the extremes.

5.2 Isolated stress fiber dynamics

Let us now consider SF dynamics in isolation. SF rheology is determined by five parameters: the elastic resistance K_E(proportional to the Young's modulus), bending resistance K_B, viscous resistance ξ, contractile stall force F_s, and free velocity of myosin per unit length v_0. If the bending coefficient K_B is small, the fast process is that of length change. Suppose there is no myosin activity, and let the change in length over time be given by $\ell(t) = L_0 - L(t)$, where L_0 is the rest length of the

fiber. Approximately, in short times, this change in length obeys the ordinary differential equation

$$\frac{\xi}{L_0}\frac{d\ell}{dt} + \frac{K_E}{L_0}\ell = 0$$

which has solution $\ell(t) = \ell_0 \exp(-t/\tau_L)$ for an initial deformation ℓ_0. Here, the timescale of length relaxation τ_L is given by $\tau_L = \xi/K_E$, reflecting, intuitively, that larger ξ(higher viscous resistance to fast deformation) and smaller K_E(lower elastic resistance to large deformation) increase the timescale of length relaxation. Including contractile forces adds an additional term in the differential equation for the change in length:

$$\frac{\xi}{L_0}\frac{d\ell}{dt} + \frac{K_E}{L_0}\ell = F_s\left(1 - \frac{1}{v_0 L_0}\frac{d\ell}{dt}\right) .$$

This contractile force contributes a forcing term, as well as complements the viscous resistance as $\xi \to \xi + F_s/v_0$. The solution to the differential equation for the change in length ℓ over time, given some initial deformation ℓ_0, is

$$\ell(t) = \frac{F_s L_0}{K_E}\left(1 - \exp(-t/\tau_L)\right) + \ell_0 \exp(-t/\tau_L)$$

where the timescale of length relaxation is now

$$\tau_L = \frac{\xi + F_s/v_0}{K_E} . \tag{25}$$

We see how smaller free velocities, i.e. the rate at which myosin traverses actin, lead to slower length change. To verify and visualize the impact of parameters on SF dynamics and τ_L, consider a SF which is initialized at rest ($L_0 = 0.5$) and allowed to contract until the elastic forces are in balance with contractile forces[3] ($\ell_\infty = F_s L_0/K_E$). Figure 4a shows the length and velocity of a contracting fiber over time in the case of predicted length relaxation timescale of $\tau_L \approx 0.092$. The length contraction of the fiber matches the predicted timescale, and we see a telescopic velocity profile where the velocity along the length of the fiber increases linearly with distance from the midpoint, as expected for an isolated viscoelastic contractile rod. Figure 4b confirms the proportionality of the timescale $\tau_L \propto 1/K_E$ and $\tau_L \propto \xi + F_s/v_0$, with our computed timescales (filled circles) matching the theoretical expectation (25) (dotted line). We can compute the retraction along the fiber (not shown here), which is constant along the length, as expected for a SF with no adhesions.

Now, suppose instead that there is no resistance to local changes in length, so the resistance to curvature governs the dynamics. To assess the impact of K_B, it is nec-

[3] This is effectively the dynamics of the length of a SF without focal adhesions after laser ablation.

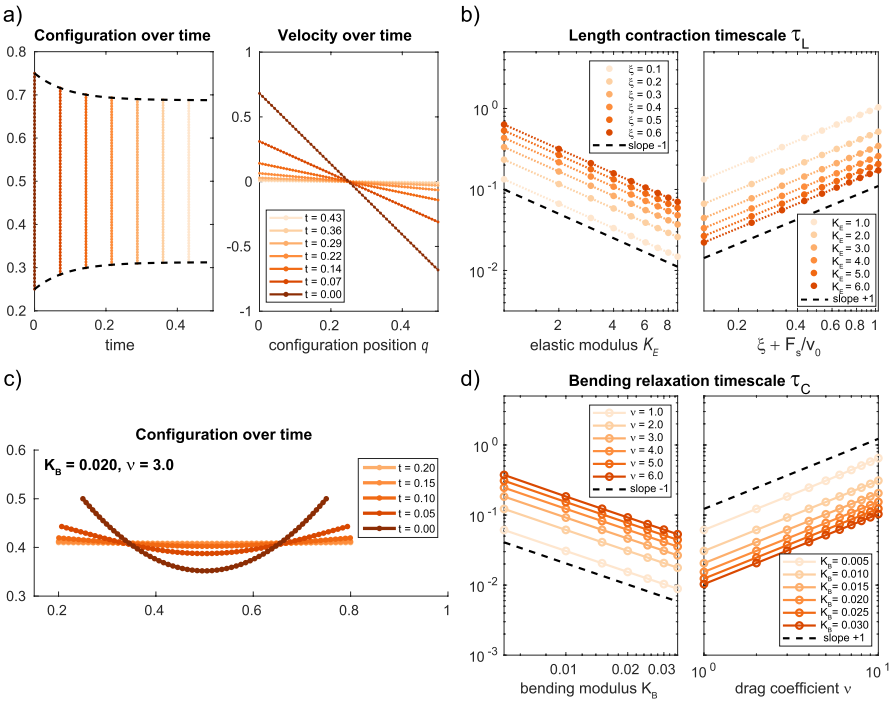

Fig. 4 **a** The configuration (left) and velocity (right) of a contracting fiber over time, for the case of $K_E = 4.0$, $\xi = 0.3$, $F_s = 1.0$, and $v_0 = 15$, where the predicted timescale of length contraction is $\tau_L \approx 0.092$. **b** The numerically calculated timescales (solid dots) of length contraction τ_L for a contracting viscoelastic fiber initialized at rest length 0.5 for variable elastic modulus K_E(left) and variable viscous resistance ξ(right), with fixed contraction parameters $F_s = 0.5$ and $v_0 = 15$. Dotted lines correspond to the theoretical prediction (25). **c** The configuration of an initially bent, roughly inextensible fiber of nondimensional length 0.6 over time, for the case of $K_E = 100.0$, $K_B = 0.02$, and $\gamma = 3.0$. **d** The numerically calculated timescales of curvature relaxation τ_C for a nearly inextensible fiber ($K_E = 100$) under constant linear drag, initialized bent at rest length 0.6 for variable bending modulus K_B(left) and variable drag coefficient ν(right)

essary to balance bending forces with a drag term, such as $\nu d\boldsymbol{X}/dt$, so that the fiber configuration obeys a PDE[4] such as

$$\nu \frac{\partial \boldsymbol{X}}{\partial t} = -K_B \frac{\partial^4 \boldsymbol{X}}{\partial q^4} \ .$$

For example, an infinitely long fiber with initial configuration $\boldsymbol{X}(q) = [q, \cos(q)]$ would have configuration $\boldsymbol{X}(q,t) = [q, \cos(q)\exp(-K_B t/\nu)]$, with curvature $\boldsymbol{C}(q,t) = \partial^2 \boldsymbol{X}/\partial q^2 = [0, -\cos(q)\exp(-K_B t/\nu)]$. In our case, the fiber is of course not infinite and has free end boundary conditions– moreover, we are interested in the regime that K_E is large so the fiber is nearly inextensible. However, in general, dimensional analysis indicates the timescale of curvature relaxation should be

[4] This PDE is with dimensions.

$$\tau_C \propto \nu L^4/K_B \tag{26}$$

where L is the fiber length. It is straightforward to demonstrate this holds for our model. Consider a symmetrically bent, inextesible fiber which has rest length $L_0 = 0.6$ as shown in Fig. 4c in brown. Figure 4c shows how, over time, the fiber straightens, with the fiber ends moving out and down while the center moves up in the domain. If one varies K_B or ν, Fig. 4d show how $\tau_C \propto 1/K_B$ and $\tau_C \propto \nu$ as expected, with computed timescales matching -1 and 1 slopes, respectively, on the log-log scale.

5.3 Stress fibers dynamics in a bulk actin network

Given our understanding of the dynamics of fibers and bulk networks in isolation, let us now consider a bulk network which is occupying a $R \times R = 50$ μm × 50 μm space, and a SF of length 37.5 μm = $0.75R$ which has thickness 1μm in diameter.[5] As SFs are often localized at the cell boundaries (Oakes et al. 2014; Ruppel et al. 2023), suppose the SF is a 5 μm= $0.1R$ distance away from the bulk network boundary. Our first aim is to characterize the dynamics of a contracting SF in this context, evaluating the dependence of the timescale of contraction on both the elastic modulus K_E and the bulk network viscosity μ with expansion viscosity $\lambda = 2\mu/3$, though any expansion viscosity $\lambda = O(\mu)$ is appropriate.

Recall that the timescale of length contraction of an isolated fiber (25) predicts an inverse relation with the fiber elastic modulus, $\tau_L \propto 1/K_E$. In the case of a fiber contracting in a fluid-like bulk network, the left plot of Fig. 5a shows this relation continues to hold approximately. For small K_E, the timescale changes a bit slower than with slope -1, because when the elastic modulus is small, the network viscous effects start to dominate the dynamics. Recall also that, for an isolated fiber, the timescale varies $\tau_L \propto \xi + F_s/v_0$, where ξ is the internal viscosity of the fiber. As some previous models of SF dynamics under laser ablation consider the cytoplasm as effectively contributing to this internal viscosity (Kassianidou et al. 2017), we wonder whether the timescale of length contraction varies like $\tau_L \propto \mu + \xi + F_s/v_0$. The right plot of Fig. 5(a) shows that it is not so straightforward, very clearly so for small K_E. For larger $K_E = 6.0$, the relation between τ_L and μ is closer to the prediction, as seen by being close to parallel with a line of slope $+1$ on the log-log plot. Meanwhile for $K_E = 1.0$, the relation is approximately $\tau_L \propto (\mu + \xi + F_s/v_0)^{0.73}$. While one might consider this deviation from the expectation to be an effect of proximity of the fiber to the bulk network boundary, these relations between K_E or μ with τ_L are conserved if the fiber is positioned differently in the bulk network (see Fig. S3 and Supplement Sect. 4 for details). Thus, as opposed to the network viscosity simply supplementing the internal viscosity of the fiber, we see that the bulk network is contributing a drag force on the fiber (of the form, for example, $F_{\text{drag}} = \nu\, d\boldsymbol{X}/dt$).

[5] Since we have observed the hydrodynamic radius of our immersed boundary method to be $O(h)$, for this problem we choose an Eulerian grid which is $h \sim \text{fiber radius/domain size} = 1/100$. Using $N_b = 60$ Lagrangian points, the discretization of the fiber $\Delta q = 0.0125$ is thus appropriately comparable to the fluid with $h = 0.01$.

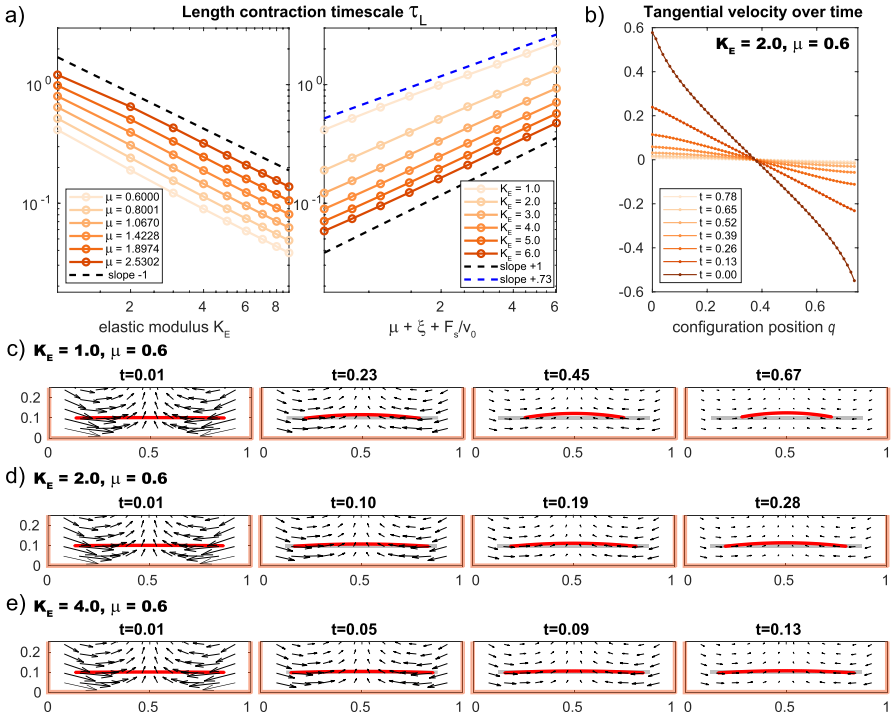

Fig. 5 **a** The numerically calculated timescales of SF contraction τ_L for a contracting viscoelastic fiber immersed in a bulk network for variable elastic modulus K_E(left) and variable bulk network viscosity μ, $\lambda = 2\mu/3$(right). The fiber is initialized at rest length 0.75 at a distance 0.1 of the edge of the domain from $x = 0.125$ to $x = 0.875$ with fixed contraction parameters $F_s = 0.5$ and $v_0 = 15$ and internal viscosity coefficient $\xi = 0.018$, the largest value for which the fixed point iteration scheme converges for all shown parameter sets. **b** The tangential velocity of a contracting fiber over time for the case of $K_E = 2.0$ and a fluid viscosity of $\mu = 0.6$. **c–e** The configuration of a contracting fiber over time with elastic moduli $K_E = 1.0, 2.0, 4.0$, immersed in a bulk actin network with viscosity $\mu = 0.6$ with the corresponding flow shown in black arrows. The quiver scale is such that a speed of 1 scales to 0.35 spatial units. Thick light orange lines mark the boundaries of the domain

Notice how in an isolated fiber, Fig. 4a showed the tangential velocity being perfectly telescopic, but a fiber immersed in a bulk network has a velocity profile, particularly in early time, which increases along the length but not linearly with position, as shown in Fig. 5b. This is the sort of profile we expect from a drag-like effect of the fluid on the fiber, the scale of which can be computed by (40) in Appendix D. However, the drag force is evidently not homogeneous throughout the bulk network, as placement of the fiber in different parts of the domain impacts the timescale of length contraction (this is seen by comparing Fig. 5 and supplement Fig. S3).

Let us now consider instead that this fiber be nearly inextensible and bent, with the same initial configuration as in Fig. 4c, placing the ends of the fiber symmetrically in the center of our domain, as shown in Fig. 6b. For an isolated fiber under constant drag, we saw a timescale which was $\tau_C \propto \nu/K_B$. If we assume that the bulk network imposes a viscous drag on the fiber, as we saw for the case of an immersed contractile fiber, we should see a timescale of curvature relaxation which is $\tau_C \propto \mu/K_B$(assum-

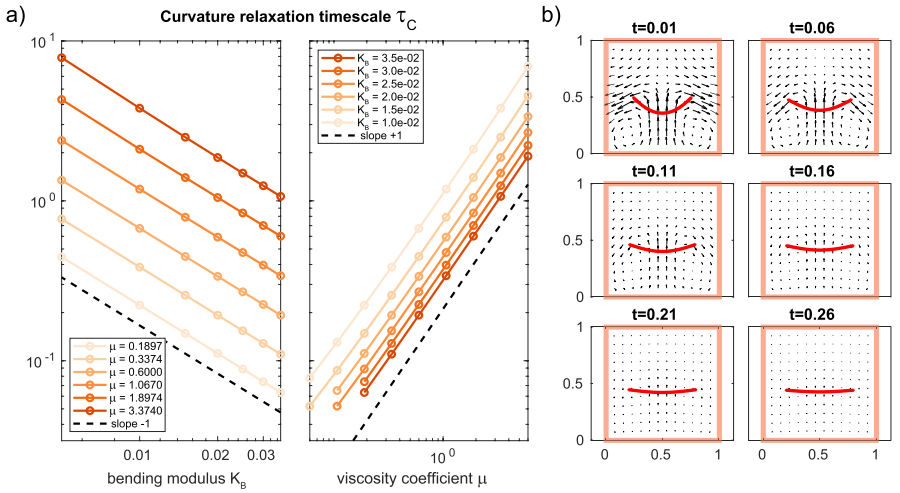

Fig. 6 **a** The numerically calculated timescales of curvature relaxation τ_C for a nearly inextensible fiber ($K_E = 100$) immersed in a bulk actin network initialized bent at rest length 0.6 for variable bending modulus K_B(left) and variable bulk network viscosity μ, $\lambda = 2\mu/3$(right). **b** The configuration of an initially bent, roughly inextensible fiber over time with elastic and bending moduli $K_E = 100.0$ and $K_B = 0.02$, immersed in a bulk actin network with viscosity $\mu = 0.1897$ with the corresponding flow shown in black arrows. The quiver scale is such that a speed of 1 scales to 0.2 spatial units. Thick light orange lines mark the boundaries of the domain

ing $\lambda = O(\mu)$). Indeed, Fig. 6a shows that the timescale of curvature relaxation decreases approximately like $\tau_C \propto 1/K_B$ for various fluid viscosities and increases approximately proportionally to the bulk network viscosity coefficient μ for various choices of bending modulus K_B. We can also look at the induced flows around the relaxing SF. In general, regardless of viscosity coefficient, Fig. 6b shows how this initial configuration of the fiber in the bulk network initially induces vortices below it in the domain as the center of the fiber moves upward while the edges of the fiber stretch out. The configuration of the fiber over time is not unlike the isolated case in Fig. 4c but the effect on the bulk network is now realized through the use of IBM.

5.4 Stress fibers dynamics in contractile actomyosin networks

It remains to address how myosin activity in bulk networks affects SF dynamics. Both in micropatterned or scaffolded cells (Kassianidou et al. 2017; Brand et al. 2017; Vignaud et al. 2021) and free non-motile cells (Gavara and Chadwick 2016; Riedel et al. 2024), SFs form on the cell periphery, embedded in the actin cortex and lining the cell contour. The cell boundary shape is then effectively a series of concave arcs between major adhesion cites (Bischofs et al. 2008; Schakenraad et al. 2020), resulting from contractility of the cytoskeleton (Zand and Albrecht-Buehler 1989; Bischofs et al. 2008). There are also SFs in the interior, which can align with the cells major axis (Gavara and Chadwick 2016; Schakenraad et al. 2020) or run diagonally through to reinforce the cell (Riedel et al. 2024). Let us consider the dynamics of four peripheral SFs embedded in a *contractile* actomyosin bulk network with high turnover of size

$R \times R = 50$ μm $\times$ 50 μm. Let the SFs be of length 37.5 μm $= 0.75R$ and thickness 0.8 μm with focal adhesions at the ends, initialized near the edges of the bulk network, specifically 5 μm away from the boundary so that the four corners of the domain have corresponding focal adhesion sites. For the bulk network, let us consider initial distributions of free and bound myosin which are steady, i.e. the contractile myosin forces are balanced with the network viscosity and exchange with freely diffusing myosin: the distributions and parameters from the top row of Fig. 3b. However, note that we do not expect this distribution to remain steady in the context of immersed SFs, as they necessarily contribute additional resistive forces and stresses. The top row of Fig. 7 shows our initial fiber and network configuration.

We expect that the inward flows of the bulk actomyosin network will initially pull the SFs inward, with the adhesions, elastic resistance, contractility, and bending resistance of the fiber eventually balancing the inward bulk flow. Figure 7 and Movie 1 show how over time the SFs stretch inward, forming concave arcs, until eventually they become stationary at approximately $T = 20$. The right column of Fig. 7 shows how around the SF, the bulk network still tends to flow inward, but over time the

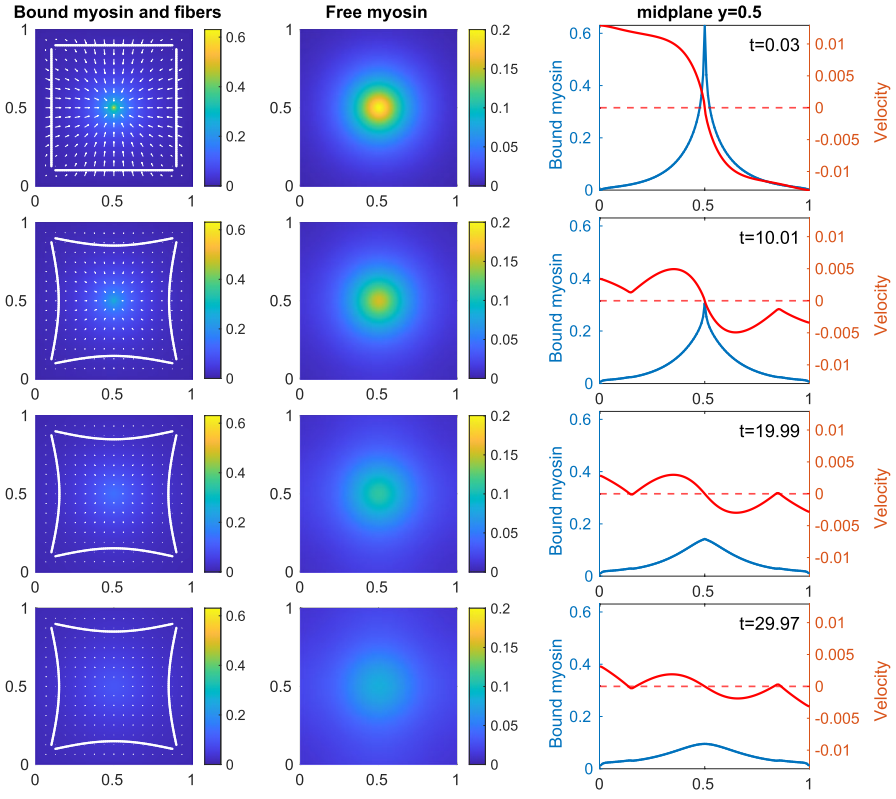

Fig. 7 The numerical solution over time, before ablation, for the case of four SFs with adhesions at their ends immersed in a bulk actomyosin network with initial bound and free myosin distributions as in the top row of Fig. 3b. The SFs have an elastic modulus $K_E = 0.25$, bending modulus $K_B = 0.001$, internal viscosity $\xi = 0.035$, contractile stall force $F_s = 0.05$, contractile free velocity $v_0 = 15$, and adhesive spring force $k_{adh} = 100$. The quiver scale takes a speed of 1 to 3 spatial units

flow speed of the network decreases due to the SF's resistance to stretch. As myosin unbinds and diffuses, this then leads to decreased myosin distribution amplitudes. Effectively, the addition of SFs disrupted the balance of contraction and diffusion in the bulk actomyosin network, resulting in a less concentrated myosin distribution. In turn, the decreased contraction of the bulk actomyosin network allows the SF to relax a little, as seen in the bottom right plot of Fig. 7 at time $t = 29.97$ where the velocity switches sign in small regimes around the SFs on the left and right.

Most studies of the ablation of peripheral SFs utilize mathematical models where the SF is considered in isolation (Besser et al. 2011; Chapin et al. 2014; Kassianidou et al. 2017; Fogelson and Mogilner 2018). Only more recently have there been models of embedded SFs (Vignaud et al. 2021; Riedel et al. 2024), but these models consider an *elastic* bulk network, while our model is more applicable in the case of high turnover of the bulk network. As such, it is unclear how SFs in the context of our case study in Fig. 7 would behave under ablation.

Suppose we ablate the center of the SF on the left side of the domain. In isolation, an ablated piece of SF should straighten and contract to a final length which is a fraction $(1 - F_s/K_E)$ of its initial unstretched length (in this case, a length $\sim 0.3R$). However, the fiber is still subject to contractile flows from the network, and ablation should impact the bulk actomyosin flows as well. Figure 8 and Movie 2 show the dynamics over time after the left SF in Fig. 7 was ablated at time $T = 30.0$. Ablation causes a sudden decrease in resistance to bulk network flow, allowing for the quick influx of flow as shown in the top right plot of Fig. 8. As the cut pieces retract, they simultaneously straighten and are "pushed aside" by the flowing bulk network, rotating inward. The bulk network flow at the center of the left boundary quickly returns to a magnitude close to its pre-fiber values (compare third row of Fig. 8 to the first row of Fig. 7). Notably, as a result of the ablation of the SF, left-right symmetry of the actomyosin network is dramatically broken, as the flows are distinctly faster on the left side than the right and the myosin distributions shift toward the right side of the domain.

In isolation, the final length of the ablated pieces of SFs should be $\approx 0.295R$, and in a passive bulk network they reach this final length with a timescale which is approximately $\tau_L \approx 4.18$ time units (see Fig. S4). However, as a result of the contractile activity of the bulk actomyosin network, the contraction of the fibers appears *faster* with a timescale of approximately $\tau_L \approx 3.86$, reaching a final length of $\approx 0.307R$, *larger* than predicted. If one is measuring the properties of the SF from such a laser ablation assay, the timescale would inherently suggest the fiber is either stiffer, with larger K_E values, or has less viscous resistance ξ than its true parameters. In addition, while the true ratio of the contractile force and elastic modulus is $F_s/K_E = 0.2$, the apparent ratio from the simulated results is instead $F_S/K_E = 0.168$, suggesting the fiber is less contractile than it is in actuality, or stiffer. As such, the activity of the bulk actomyosin network changes the apparent quantitative properties of the SFs as measured by a laser ablation experiment.

Figure 8 also demonstrates how multiple SFs interact hydrodynamically through the bulk actomyosin network. As a result of ablation of the left SF, between $t = 30$ and $t = 50$ Fig. 8 also shows how *all* the other peripheral SFs, not just the fiber on the other side, relax partially after ablation. In the rightmost column of Fig. 8, at

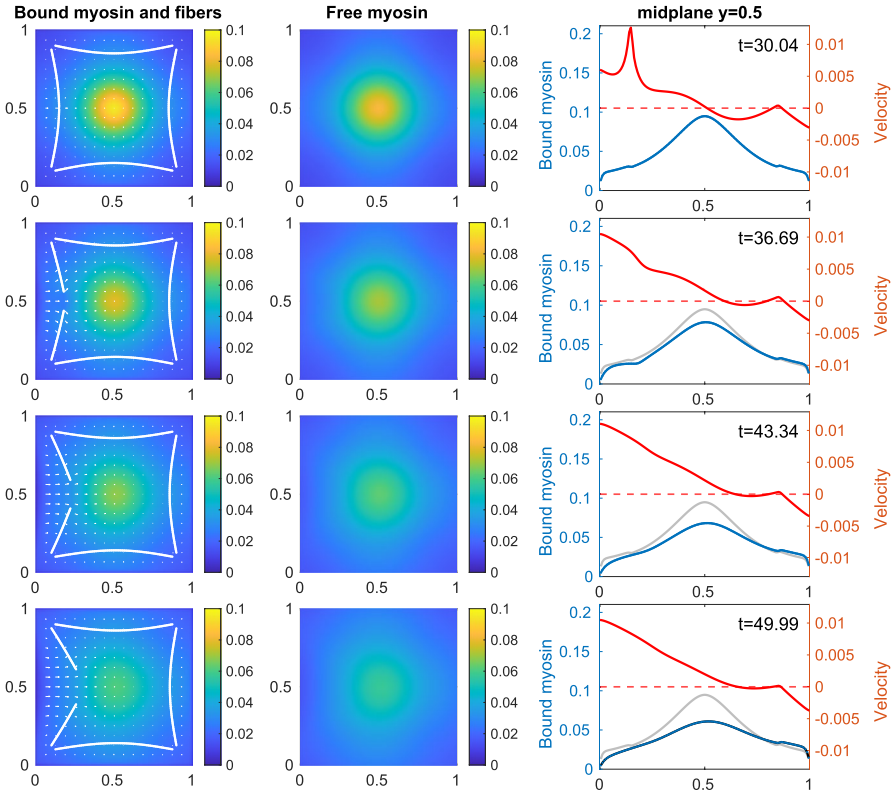

Fig. 8 Continuing from the final time of Fig. 7, the numerical solution over time after ablation of the left SF in the center at time $T = 30.0$ until final time $T = 50.0$

$t = 36.69$ the velocity of the right SF is distinctly positive and nonzero, meaning it is moving outward and relaxing, until the forces are again in balance by the final time $t = 49.99$.

6 Discussion

In this work, we have utilized a novel approach to the modeling and simulation of SFs embedded in bulk actomyosin networks with high turnover. Within such bulk networks, bound myosin induces contractile stresses and flows which are balanced by viscous resistance of the actin network and the unbinding of myosin which then diffuses freely. Through simulations, we characterized the dynamics of such contractile bulk networks in 2D, highlighting the different possible steady states and their dependence on mechanical and kinetic parameters. We then coupled the dynamics of the bulk network with the mechanics of individual SFs through the IBM, allowing the use of SF viscoelastic models which have been used extensively to explore isolated SF dynamics. Our simulations of individual SFs in passive bulk networks

demonstrated the relevance of hydrodynamic effects of both the fiber mechanics on the network as well as the network flows and boundaries on the fiber.

When considering the case study of four contractile SFs with adhesions embedded in a contractile bulk network, we demonstrated how SFs effectively interact across cell-sized distances as a result of their embedding in the bulk actomyosin network. Ablation of one SF resulted in reduced tension in the other SFs, in agreement with experiments which have shown that laser ablation of a SF can lead to tension release across SFs in the cell (Kassianidou et al. 2017; Vignaud et al. 2021). In addition, the other SFs exhibited relaxed bending, replicating experimental results where SFs appear less bent in response to a change in tension elsewhere in the cell network (Kumar et al. 2006). The perturbation of one SF also yielded a symmetry break in the bulk network. Of course, comparison of such model results with experiments is made complicated because SFs form an interlinked network in cells, both at the cell boundary and throughout the interior (Kassianidou et al. 2017; Vignaud et al. 2021; Riedel et al. 2024). As such, features such as fiber bending due to contraction near boundaries in Fig. 5 and the dramatic inward turning of ablated SF pieces in Fig. 8 would not be expected in cellular conditions. Nonetheless, our model can reproduce physiological phenomena, such as the curving inward of SFs at the boundary (Kassianidou et al. 2017; Brand et al. 2017; Vignaud et al. 2021; Riedel et al. 2024) and the impact of SFs with focal adhesions on lamellipodial flow, discussed in the Supplement with reference to experimental results in Alexandrova et al. (2008).

To our knowledge, this is the first study to consider the simulation of SFs in bulk contractile actomyosin networks with high turnover, particularly through the use of the IBM. The advantage of utilizing the IBM lies in how it couples the SF and active bulk network. We chose here to consider a SF model which corresponds to models of individual SF dynamics under ablation; however, the IBM formulation allows us to easily change the rheology of the SF, and even introduce heterogeneity along the length, as it only requires modification of the force calculations in the Lagrangian fiber framework. We are also able to consider multiple fibers of differing lengths and properties. Unlike previous works, we are thus able through our model to investigate questions as how different contractile higher-order actomyosin structures affect each other.

The primary computational constraint on the approach presented here is that the Eulerian grid size of immersed fibers should be on the order of the true radius of the fibers. In 2D, it was sufficient to consider grid sizes $h \sim 1/200 - 1/100$ to simulate fibers of realistic thickness. However, it quickly becomes computationally intractable to consider very thin fibers. Additionally, in the 2D model, our implementation only allows us to consider small values for the internal fiber viscosity when the fiber is embedded in the bulk. However, in 3D we can mimic the approach of Maxian and Peskin (2020) to leverage an analytical result regarding the drag on a sphere immersed in the fluid, instead considering a fiber equation of motion given by

$$\frac{d\boldsymbol{X}}{dt}(q,t) = \boldsymbol{S}^{*}\left(\boldsymbol{X}\right)\boldsymbol{u} + \frac{1}{\gamma}\boldsymbol{F}(q)\ . \tag{27}$$

where γ is a function of the hydrodynamic radius r_h, the true radius of the fiber a, and the viscosities of the actin network μ and λ:

$$\gamma = 108\pi \frac{\mu\lambda\,(3\lambda + 4\mu)}{(3\lambda + 10\mu)\,(6\lambda + 11\mu)} \frac{r_h a}{r_h - a} = 108\pi\eta \frac{r_h a}{r_h - a}\ . \tag{28}$$

This modified equation of motion (27) would then allow one to simulate the dynamics of thin SFs with computationally accessible coarser grid sizes, retaining the appropriate drag on the SFs. Moreover, this modified IBM formulation (27) is advantageous in contexts where the focus is on bulk flows on larger scales than the fiber radius a. For full details, see Appendix D. Prior work in the Stokes case (Maxian and Peskin 2020) and our preliminary work for our model indicates that this modified algorithm dramatically reduces the constraints on both Eulerian grid size and internal fiber viscosity. Alternatively, we could implement a semi-implicit method similar to Strychalski and Guy (2012). The benefit of this computational work in 2D is that we have characterized the effects of the various bulk actomyosin parameters and SF parameters. The 2D case also demonstrates the relevance of bulk flows at large scales, as opposed to small scale flows resolved by fine meshes. So, we are poised to apply our model to investigate the dynamics of SFs in bulk networks in 3D, where we can take advantage of our proposed modified IBM algorithm (27) and use parameters informed by our work in 2D.

For computational simulation of suspensions of fibers in low Reynolds number flows, a common alternative modeling approach to IBM is to employ a boundary-integral formulation using slender body theory (Keller and Rubinow 1976; Tornberg and Shelley 2004), which has been used for example to capture microtubule dynamics in the mitotic spindle (Nazockdast et al. 2017) and the bundling dynamics of actin filament networks (Maxian et al. 2021). Notably, these methods consider fibers in Stokes-like fluids, capturing fiber dynamics by employing fundamental solutions of the Stokes equation (e.g. the Stokeslet tensor). To our knowledge, there is no equivalent approach for the type of active, compressible viscous fluid we use here to capture the bulk actomyosin dynamics. The benefit of an IBM approach is it permits flexibility in choice of both the fiber and fluid models.

In this work, we consider previously published simplified models for SFs, which assume that they are homogeneous along their length and that their properties do not change with time. However, experiments have shown that there is heterogeneity in these properties along their length (Costa et al. 2002; Peterson et al. 2004). Additionally, SFs are dynamic, undergoing reinforcement and repair under tension (Burridge and Guilluy 2016), as well as disassembly or rearrangement on long timescales (Vignaud et al. 2021). In this work, we have also neglected the impact of adhesions along the length of the fibers, but some laser ablation experiments suggest the existence of such adhesions (Besser et al. 2011; Kassianidou et al. 2017). To include some of these complexities would require further modeling efforts, but in general our formulation allows for the easy modification of the SF rheology so long as one can appropriately discretize the relevant forces on the Lagrangian grid. In future work, in application of this model to study a particular experimental question, we intend to consider different fiber rheologies to determine the appropriate description depending

on the problem's timescale and components. In utilizing this model formulation for future work, our characterization of the dynamics and interplay between parameters in lower dimensions will inevitably be informative and instructive in full 3D studies of higher complexity.

Appendix A: How K_E relates to the young modulus Y of the fiber

Note that the elastic energy of the fiber (9) is in terms of parameter K_E with dimension of force, unlike a traditional spring constant, which has dimension of force over length. To contextualize what K_E represents, suppose that our fiber has some Young's modulus Y, which is

$$Y = \frac{\text{stress}}{\text{strain}} = \frac{\sigma}{\varepsilon}\,.$$

The axial stress σ is simply the force over the cross-sectional area A of the fiber: $\sigma = F/A$.

Suppose then that the fiber is stretched from rest length L_0 to new length $L = L_0 + \Delta L$, resulting in strain $\varepsilon = \Delta L/L_0$. The magnitude of the force F from this strain is the fiber tension, and our constitutive law (10) is that tension is a function of the stretch ratio $\nu = \|\partial \boldsymbol{X}/\partial q\|$:

$$T(\nu) = K_E\,(\nu - 1)\ .$$

In the case of a stretched fiber, $\nu = L/L_0 = 1 + \Delta L/L_0$, so the tension, and thus force, is

$$F = K_E \frac{\Delta L}{L}\,.$$

This yields a direct proportionality between our elastic measure K_E and the fiber Young's modulus:

$$Y = \frac{\sigma}{\varepsilon} = \frac{F}{A}\frac{1}{\varepsilon} = K_E \frac{\Delta L}{L}\frac{1}{A}\frac{L}{\Delta L} \Longrightarrow K_E = Y A\,.$$

This shows that K_E is a proxy for the Young's modulus; moreover, it demonstrates that K_E is independent of the total length of the fiber L. In the context of spatially discretizing the fiber, K_E's independence with respect to length means that one can easily implement a non-uniform discretization along the fiber– the same K_E "spring constant" will apply throughout all of the fiber.

Appendix B: Numerical scheme for bulk actomyosin network model

We solve the network force balance Eq. (6) and myosin density dynamics Eq. (4) with boundary conditions (3) and (5) on 2D rectangular domains $\Omega = [L_a, L_b] \times [L_c, L_d]$ which are of $O(1)$ in size as a result of nondimensionalization by true domain size R. We consider an Eulerian grid with $N_x \times N_y$ cells, utilizing a staggered Arakawa C-grid (see Fig. 9) where the myosin densities m and b are stored at the interior of grids and the fluid velocity components are stored at their corresponding cell edges.

We solve the network force balance equation using a second-order finite difference scheme. Recall that we denote the resultant discretized force balance equation as

$$(\lambda + \mu/3)\, \boldsymbol{D}\, (\boldsymbol{D} \cdot \boldsymbol{u}) + \mu L \boldsymbol{u} = -\boldsymbol{D} m + \boldsymbol{u} + \boldsymbol{f} \qquad (21)$$

where $\boldsymbol{D}$ is the discretized Del operator and L is the discretized Laplacian. The numerical scheme boils down to solving a linear system $Aw = f$, where A is of size

$$\left[(N_x + 2)\,(N_y + 1) + (N_x + 1)\,(N_y + 2)\right]^2 \sim 4 N_x^2 N_y^2$$

and is banded with upper and lower bandwidth which are approximately

$$2\left[(N_x + 2)\,(N_y + 1) + (N_x + 1)\,(N_y + 2)\right] \sim 2 N_x N_y\,.$$

In MATLAB, we solve this linear system using backslash.

The myosin distributions m and b are solved in time at the interior of cells in the Arakawa C-grid with a finite volume approach. The advection-reaction equation in (4) for bound myosin m is solved using the first-order Corner Transport Upwind (CTU) finite volume scheme, which has stability condition

$$\max\left(\frac{|u|\,\Delta t}{\Delta x}, \frac{|v|\,\Delta t}{\Delta y}\right) < 1\,. \qquad (29)$$

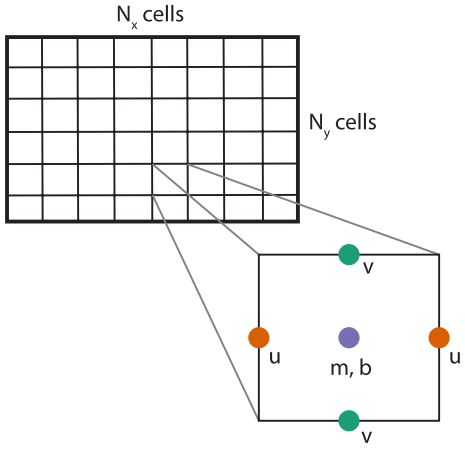

Fig. 9 Depiction of a standard Arakawa C grid, denoting where velocity $\boldsymbol{u} = < u, v >$ components u (orange) and v (green) are solved, as well as myosin densities m and b (purple)

This takes the strictest CFL stability condition between the x and y direction. The free myosin density b obeys a diffusion–reaction Eq. (4), which is solved to second order using the unconditionally stable Crank-Nicolson method.

In sum, the bulk network dynamics are solved to first order. We validated our numerical schemes in smooth cases using manufactured solutions for a variety of parameter choices, confirming second or first order convergence of each respective component individually, as well as the first order convergence of the entire scheme. We only see drops in accuracy for the network flow when the nondimensional viscosities μ and λ are very large, reflecting that solutions of (6) are only unique *up to a constant* in the absence of myosin forcing or drag terms. In non-smooth cases of myosin distributions, we see a predicted small decrease in convergence rate and evidence of artificial diffusion, which is indeed the primary numerical artifact of the CTU scheme for advection equations. However, additional diffusion is not of particular concern, as in our biological application it effectively contributes to the action of the freely diffusing myosin population. Additionally, achieving several digits of accuracy for small grid sizes is not absolutely necessary, as 1-2 digits of relative accuracy is sufficient in the context of cell biology applications where experimental data is noisy and highly heterogeneous between systems. Overall, we utilize timesteps at or smaller than 10^{-3}, and thus nearly always operate in the observed asymptotically convergent regimes of our numerical scheme for the bulk actomyosin network.

Appendix C: Spatial discretization of fiber forces

Elastic forces

We will consider N_b Lagrangian points $\boldsymbol{X}_k$ along the fiber to approximate its configuration $\boldsymbol{X}(q)$. The discretized elastic energy of the fiber (9) takes the form

$$E_e\left[\boldsymbol{X}_1,\ldots,\boldsymbol{X}_{N_b}\right] = \frac{K_E}{2}\sum_{k=1}^{N_b-1}\left(\frac{\|\boldsymbol{X}_{k+1}-\boldsymbol{X}_k\|}{\Delta q_{k+1/2}}-1\right)^2\Delta q_{k+1/2} \tag{30}$$

where the energy has become equivalent to the sum of the elastic energies of a series of springs between the Lagrangian points, each with rest length $\Delta q_{k+1/2}$. This has an associated discretized elastic *force* (not force density) at each node $\boldsymbol{X}_k$ given by

$$\boldsymbol{F}_k^e = -\frac{\partial E_e}{\partial \boldsymbol{X}_k} = T_{k+1/2}\boldsymbol{\tau}_{k+1/2} - T_{k-1/2}\boldsymbol{\tau}_{k-1/2} \tag{31}$$

with tension between nodes k and $k+1$ given by

$$T_{k+1/2} = K_E\left(\frac{\|\boldsymbol{X}_{k+1}-\boldsymbol{X}_k\|}{\Delta q_{k+1/2}}-1\right) \tag{32}$$

and unit tangent defined by

$$\boldsymbol{\tau}_{k+1/2} = \left(\boldsymbol{X}_{k+1} - \boldsymbol{X}_k\right) / \left\|\boldsymbol{X}_{k+1} - \boldsymbol{X}_k\right\| . \tag{33}$$

In the case when the fiber ends are connected, i.e. there is a fiber loop, it is straightforward to adjust the $\boldsymbol{F}_k$ at the ends such as to consider the tension and unit tangent between the first $\boldsymbol{X}_1$ and last point $\boldsymbol{X}_{N_b}$. Otherwise, note that there will be no balance of the tension at the ends.

Bending forces

In the case of a bending fiber, for simplicity we assume that the discretization has all equal reference lengths Δq. The fiber's bending energy (13) can be discretized as

$$E_b\left[\boldsymbol{X}_1, \ldots, \boldsymbol{X}_{N_b}\right] = \frac{K_B}{2} \sum_{k=2}^{N_b-1} \left\|\boldsymbol{C}_k\right\|^2 \Delta q \tag{34}$$

where $\boldsymbol{C}_k$ is the discrete curvature, defined only at interior points:

$$\boldsymbol{C}_k = \frac{\boldsymbol{X}_{k+1} - 2\boldsymbol{X}_k + \boldsymbol{X}_{k-1}}{(\Delta q)^2} , \qquad k = 2, \ldots, N_b - 1 . \tag{35}$$

This energy (34) has an associated discretized elastic force at each node $\boldsymbol{X}_k$ given by

$$\boldsymbol{F}_k^b = -\frac{\partial E_b}{\partial \boldsymbol{X}_k} = -K_b \frac{\boldsymbol{C}_{k-1} - 2\boldsymbol{C}_k + \boldsymbol{C}_{k+1}}{\Delta q} . \tag{36}$$

At the interior, this is effectively a discretization of the fourth derivative of $\boldsymbol{X}$ with respect to q (except this is *true* force as opposed to force density, so it is missing an additional multiplier $1/\Delta q$). Near the ends of the fiber, the discretization reflects the free-end nature of the fiber. In the case that the fiber ends are connected, i.e. there is a fiber loop, it is straightforward to define curvature at $k = 1$ or $k = N_b$ and apply the same discretized force (36).

Viscous forces

Recall that in discretizing the elastic fiber, we showed that the total energy is equivalent to the sum of the elastic energy of a series of springs between the Lagrangian points. In discretizing a viscoelastic fiber which behaves like a Kelvin-Voigt solid, we similarly consider instead a series of Kelvin-Voigt elements between the Lagrangian points. Consider the element between the k and $k + 1$ Lagrangian points. The viscous force of at $\boldsymbol{X}_k$ due to this element is a discretization of (15) with unit tangent direction $\boldsymbol{\tau}_{k+1/2}$:

$$\begin{aligned}\boldsymbol{F}_k^v &= \frac{\xi}{\Delta q_{k+1/2}} \frac{\partial}{\partial t} \|\boldsymbol{X}_{k+1} - \boldsymbol{X}_k\| \, \boldsymbol{\tau}_{k+1/2} \\ &= \frac{\xi}{\Delta q_{k+1/2}} \left[(\boldsymbol{U}_{k+1} - \boldsymbol{U}_k) \cdot \boldsymbol{\tau}_{k+1/2}\right] \boldsymbol{\tau}_{k+1/2} \,.\end{aligned} \tag{37}$$

There is also an analogous force on the Lagrangian point k coming from the element between the $k-1$ and k Lagrangian points.

Myosin forces

We can discretize the myosin force (16) for each subunit of the fiber, taking the current length as $L \to \|\boldsymbol{X}_{k+1} - \boldsymbol{X}_k\|$ and the rest length as $L_0 \to \Delta q$. Consider the element between the k and $k+1$ Lagrangian points. The resultant contractile force due to this element is in the tangent direction $\boldsymbol{\tau}_{k+1/2}$:

$$\begin{aligned}\boldsymbol{F}_k^m &= F_s \left(1 + \frac{1}{v_0 \Delta q_{k+1/2}} \frac{d}{dt} \|\boldsymbol{X}_{k+1} - \boldsymbol{X}_k\|\right) \boldsymbol{\tau}_{k+1/2} \\ &= F_s \left(\boldsymbol{\tau}_{k+1/2} - \boldsymbol{\tau}_{k-1/2}\right) + \frac{F_s}{v_0 \Delta q_{k+1/2}} \left[(\boldsymbol{U}_{k+1} - \boldsymbol{U}_k) \cdot \boldsymbol{\tau}_{k+1/2}\right] \boldsymbol{\tau}_{k+1/2} \,.\end{aligned} \tag{38}$$

Note that this is similar to the discretized fiber viscous resistance force (37). This is a result of both this myosin force and the viscous resistance depending on the rate of change in the length of a section of the fiber.

Appendix D: Modified IBM for 3D networks

Following the approach of Maxian and Peskin (2020), when looking at SFs in 3D bulk networks, we can leverage an analytical result regarding the drag on an sphere immersed in the fluid, instead considering a fiber equation of motion given by

$$\frac{d\boldsymbol{X}}{dt}(q,t) = \boldsymbol{S}^* \left(\boldsymbol{X}\right) \boldsymbol{u} + \frac{1}{\gamma} \boldsymbol{F}(q) \,. \tag{27}$$

One can choose γ by solving the equivalent of a Stokes drag in the case of our compressible fluid, meaning calculating the drag force on a sphere of radius a immersed in some background flow U. The dimensional actin network force balance equation in this case would be

$$(\lambda + \mu/3) \nabla (\nabla \cdot \boldsymbol{u}) + \mu \Delta \boldsymbol{u} = \zeta \boldsymbol{u} \,.$$

Now, non-dimensionalizing this equation by the size of the sphere a and the background flow speed U yields

$$\frac{\lambda+\mu/3}{\zeta a^2}\nabla\left(\nabla\cdot\boldsymbol{u}\right)+\frac{\mu}{\zeta a^2}\Delta\boldsymbol{u}=\boldsymbol{u}\,.$$

As in Sect. 2.1, we once again identify μ/ζ as ℓ_0^2, the hydrodynamic length squared. Assuming λ and μ are of approximately the same scale, the fluid equation becomes

$$O(1)\nabla\left(\nabla\cdot\boldsymbol{u}\right)+\Delta\boldsymbol{u}=\left(\frac{a}{\ell_0}\right)^2\boldsymbol{u}\,.$$

Note the following: generally, the hydrodynamic length for the cytoplasm is comparable to cell sizes (Mayer et al. 2010). The size of the sphere, determined by radius a, in our context would correspond to the thickness of the fiber, which has variable widths often smaller than 0.5 μm (Livne and Geiger 2016) but could potentially be as large as a micron in width (Buenaventura et al. 2024). Even in this latter case, $a/\ell_0\sim 10^{-2}$, making the drag term of the order $O\left(10^{-4}\right)$, which is much smaller than the order 1 terms on the left-hand-side. As such, the contribution of external drag to the total drag on the sphere is approximately negligible, and we can instead solve the problem:

$$\begin{aligned}\left(\lambda+\mu/3\right)\nabla\left(\nabla\cdot\boldsymbol{u}\right)+\mu\Delta\boldsymbol{u}=0 &\quad \forall\, r>a\\ \boldsymbol{u}=\boldsymbol{0} &\quad \text{on } r=a\\ \boldsymbol{u}=\boldsymbol{U} &\quad \text{as } r\to\infty\,.\end{aligned}$$

Due to the inherent spherical symmetry, let our ansatz for the flow field be that it takes the form

$$\boldsymbol{u}\left(r,\theta\right)=f(r)\cos\left(\theta\right)\hat{\boldsymbol{r}}+g(r)\sin\left(\theta\right)\hat{\boldsymbol{\theta}}\,. \tag{39}$$

The specific $f(r)$ and $g(r)$ which satisfy the boundary conditions are

$$\begin{aligned}f(r)&=U\frac{3\lambda}{\left(\lambda+10\mu/3\right)\left(2\lambda+11\mu/3\right)}\left[\left(2\lambda+11\mu/3\right)-3\left(\lambda+4\mu/3\right)\frac{a}{r}+\left(\lambda+\mu/3\right)\frac{a^3}{r^3}\right],\\ g(r)&=U\frac{3\lambda}{4\left(\lambda+10\mu/3\right)\left(\lambda+11\mu/6\right)}\left[-2\left(2\lambda+11\mu/3\right)+3\left(\lambda+7\mu/3\right)\frac{a}{r}+\left(\lambda+\mu/3\right)\frac{a^3}{r^3}\right].\end{aligned}$$

Recall that the viscous stress on the fluid is

$$\boldsymbol{\sigma}=\left(\lambda-2\mu/3\right)\left(\nabla\cdot\boldsymbol{u}\right)\boldsymbol{I}+\mu\left(\nabla\boldsymbol{u}+\nabla\boldsymbol{u}^T\right)=\left(\lambda-2\mu/3\right)\left(\nabla\cdot\boldsymbol{u}\right)\boldsymbol{I}+\mu\boldsymbol{\tau}\,.$$

We integrate the stress over the surface of the sphere to find the resultant drag force. By symmetry, as in the Stokes case, the force should be in the $\hat{\boldsymbol{z}}$ direction:

$$\begin{aligned}\boldsymbol{F}\cdot\hat{\boldsymbol{z}} &= \int\int_S \hat{\boldsymbol{r}}\cdot\boldsymbol{\sigma}\cdot\left(\cos\theta\hat{\boldsymbol{r}}-\sin\theta\hat{\boldsymbol{\theta}}\right)\, a^2\sin\theta d\theta d\phi \\ &= 2\pi a^2\int_0^\pi \left[\left(\mu\tau_{rr}+(\lambda-2\mu/3)\,\nabla\cdot\boldsymbol{u}\right)\cos\theta-\left(\mu\tau_{r\theta}+(\lambda-2\mu/3)\,\nabla\cdot\boldsymbol{u}\right)\sin\theta\right]\sin\theta d\theta \\ &= \underbrace{2\pi a^2\mu\int_0^\pi\left(\tau_{rr}\cos\theta\sin\theta-\tau_{r\theta}\sin^2\theta\right)d\theta}_{\text{viscous shear part}}+\underbrace{2\pi a^2\left(\lambda-2\mu/3\right)\int_0^\pi\nabla\cdot\boldsymbol{u}\left(\cos\theta-\sin\theta\right)\sin\theta d\theta}_{\text{viscous expansion part}}\,.\end{aligned}$$

Notably, we clearly see the contributions to the drag force due to resistance to expansion/compression versus shear. Solving the above integrals, we find the drag force velocity relationship

$$F_{\text{drag}} = 108\pi aU\frac{\mu\lambda\left(3\lambda+4\mu\right)}{\left(3\lambda+10\mu\right)\left(6\lambda+11\mu\right)} = 108\pi\eta aU \tag{40}$$

and notice the similarity with the case of Stokes flow, where $F_{\text{drag}} = 6\pi\mu aU$. Then, in order to choose γ, suppose we split (40) into two parts: an IBM part with the hydrodynamic radius r_h and a Stokes part with a correction radius r_c:

$$\boldsymbol{U} = \frac{\boldsymbol{F}}{108\pi\eta r_h}+\frac{\boldsymbol{F}}{108\pi\eta r_c}\,.$$

For equivalency with (40), set $r_c = r_h a/(r_h-a)$. Note that so long as $r_h \geq a$, which is favorable as it means h can be larger than the true radius, then the correction radius is positive as necessary. Identifying the first term on the right-hand-side as the velocity component from the IBM, we recover (27):

$$\boldsymbol{U} = \frac{d\boldsymbol{X}}{dt} = \boldsymbol{S}^*\left(\boldsymbol{X}\right)\boldsymbol{u}+\frac{1}{\gamma}\boldsymbol{F}(q) \qquad \text{with} \quad \gamma = 108\pi\eta r_c\,.$$

As expected, the slip coefficient γ depends on both viscosity coefficients, though not in a manner which is directly proportional.

Recall that γ is calculated in the case of an infinite domain– however, generally we are interested in a finite domain with no-stress boundary conditions on the actin network. In the same manner that we found the environmental drag term is approximately negligible $\zeta\boldsymbol{u}\approx\boldsymbol{0}$(because the fiber radius is much smaller than the hydrodynamic length), generally the domain size (on the same order as the hydrodynamic length) is much larger than the fiber radius, making contributions from the far field boundary conditions small. As such, so long as the fiber is not too close to the boundary, (27) approximately holds.

Appendix E: Temporal discretization of immersed boundary numerical scheme

Four-point $\delta_{\Delta x,\Delta y}$ function

The four-point $\delta_{\Delta x,\Delta y}$ function is defined as

$$\delta_{\Delta x,\Delta y}(\boldsymbol{x}) = \frac{1}{\Delta x \Delta y}\phi\left(\frac{x}{\Delta x}\right)\phi\left(\frac{y}{\Delta y}\right) \tag{41}$$

where $\phi(r)$ is given by

$$\begin{aligned}
\phi(r) &= \frac{3-2r+\sqrt{1+4r-4r^2}}{8} \quad \text{on } 0 \le r \le 1 \\
\phi(r-2) &= \frac{1}{2} - \phi(r) \\
\phi(r-1) &= \frac{1}{2}\left(r-\frac{1}{2}\right) + \phi(r) \\
\phi(r+1) &= \frac{1}{2}\left(-r+\frac{3}{2}\right) - \phi(r)
\end{aligned}$$

which is nonzero on the interval $r \in (-2, 2)$ and is otherwise zero. The discretized delta function $\delta_{\Delta x,\Delta y}$ will effectively "spread" or "interpolate" a field (depending on use) to the closest four points in a 1D domain. Figure 10 shows $\phi(r)$ as a function of r and the representative interpolation effect of the discretized delta function for an immersed boundary point in a 2D domain with a regular grid of size $\Delta x = \Delta y = 0.01$. Note that since we consider a staggered grid for the bulk actomyosin network, the x component of the elastic force is spread onto the u-component grid points and the y component of the elastic force is spread onto the v-component grid points, and vice versa for interpolation of the fluid to the fiber.

Timestepping in traditional IBM

In traditional IBM, immersed structures are typically purely elastic, in which case we can solve for the fiber configuration at each timestep as follows:

1. Given a fiber configuration at timestep n, denoted as $\boldsymbol{X}^n$, calculate the forces on the fiber:

$$\boldsymbol{F}_k^n = \boldsymbol{F}_k^e + \boldsymbol{F}_k^b + \boldsymbol{F}_k^a .$$

2. Spread the forces to the fluid:

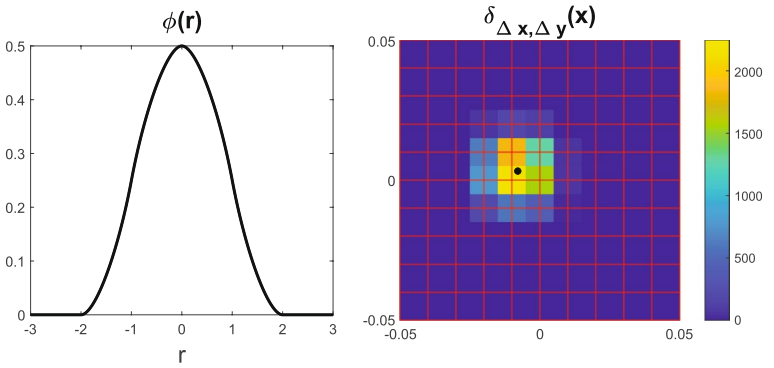

Fig. 10 (Left) The interpolation function $\phi(r)$ for $r \in [-3, 3]$. (Right) Depiction of the "spreading" effect of the four-point delta function (41) for an immersed point (black dot) on a grid of size $\Delta x = \Delta y = 0.01$(red lines)

$$\boldsymbol{f}^n = \boldsymbol{S}\boldsymbol{F}^n \,.$$

3. Solve for the fluid velocity $\boldsymbol{u}^n$ using (21).
4. Interpolate the fluid velocity to the Lagrangian points:

$$\boldsymbol{U}^n = \boldsymbol{S}^* \boldsymbol{u}^n \,.$$

5. Update the fiber configuration using, for example, a forward Euler timestep:

$\boldsymbol{X}^{n+1} = \boldsymbol{X}^n + \Delta t \boldsymbol{U}^n$ ·However, suppose we consider a viscous resistive force $\boldsymbol{F}^v$ or velocity-dependent contractile force $\boldsymbol{F}^m$. Then to calculate the forces in step 1 requires knowing the velocity, which is only solved for in step 4 above. Instead, one can solve for both the configuration $\boldsymbol{X}^n$ *and* the fiber velocity $\boldsymbol{U}^n$ using fixed point iteration. See Appendix E.2.1 for details.

Timestepping using fixed point iteration

We solve the immersed boundary system over time as follows:

- *Initialization*: At initial time $t_0 = 0$, we know the fiber configuration, i.e. $\boldsymbol{X}_k^0$ for each Lagrangian point, and the fiber spring rest lengths $\Delta q_{k+1/2}$. Guess that the initial fiber velocity is zero, i.e.

$$\boldsymbol{U}_k^{0,(0)} = 0 \quad \forall \; k \,.$$

At other timesteps t_n, we know the two fiber configurations $\boldsymbol{X}_k^n$ and $\boldsymbol{X}_k^{n-1}$. Guess that the fiber velocity at this timestep is

$$\boldsymbol{U}_k^{n,(0)} = \boldsymbol{U}_k^{n-1} = \frac{\boldsymbol{X}_k^n - \boldsymbol{X}_k^{n-1}}{\Delta t}\,.$$

At each FPI step $m = 1, 2, 3, \ldots$: Given the fiber velocity guess $\boldsymbol{U}_k^{n,(m-1)}$1.

Calculate the forces on the fiber:

$$\begin{aligned}\boldsymbol{F}_k^{n,(m-1)} = \boldsymbol{F}_k^e + \boldsymbol{F}_k^a + \boldsymbol{F}_k^b + \boldsymbol{F}_k^v\left(\boldsymbol{U}_{k-1}^{n,(m-1)}, \boldsymbol{U}_k^{n,(m-1)}, \boldsymbol{U}_{k+1}^{n,(m-1)}\right)\\ + \boldsymbol{F}_k^m\left(\boldsymbol{U}_{k-1}^{n,(m-1)}, \boldsymbol{U}_k^{n,(m-1)}, \boldsymbol{U}_{k+1}^{n,(m-1)}\right)\,.\end{aligned}$$

(Note that we omit denoting the dependence of forces on $\boldsymbol{X}_k^n$).

2. Spread the forces to the fluid

$$\boldsymbol{f}^{n,(m-1)} = \boldsymbol{S}\boldsymbol{F}^{n,(m-1)}\,.$$

3. Solve for the fluid velocity $\boldsymbol{u}^{n,(m-1)}$ using (21).
4. Take an explicit timestep to find the next approximate fiber configuration and velocity:

$$\frac{\boldsymbol{X}^{n+1,(m)} - \boldsymbol{X}^n}{\Delta t} = \boldsymbol{U}^{n,(m)} = \boldsymbol{S}^*\left(\boldsymbol{X}^n\right)\boldsymbol{u}^{n,(m-1)} = \boldsymbol{S}^*\left(\boldsymbol{X}^n\right)\boldsymbol{u}\left(\boldsymbol{X}^n, \boldsymbol{U}^{n,(m-1)}\right)\,.$$

- *STOP* iterating when

$$\frac{\left\|\boldsymbol{X}_k^{n,(m)} - \boldsymbol{X}_k^{n,(m-1)}\right\|}{\left\|\boldsymbol{X}_k^{n,(m-1)}\right\|} < \text{tol}$$

for some tolerance tol, which we choose to be tol$= 10^{-5}$. Let this final fiber position be the updated configuration, and set the fluid and fiber velocities at timestep t_n to be

$$\boldsymbol{u}^n = \boldsymbol{u}^{n,(m)} \qquad \text{and} \qquad \boldsymbol{U}^n = \boldsymbol{U}^{n,(m)} = \frac{\boldsymbol{X}^{n+1,(m)} - \boldsymbol{X}^n}{\Delta t}\,.$$

Supplementary Information The online version contains supplementary material available at https://doi.org/10.1007/s00285-025-02245-6.

Acknowledgements We thank O. Maxian, W. Strychalski, and C. Copos for useful suggestions. This work was supported by National Science Foundation grants DMS 1953430 and 2052515.

Author contributions All authors contributed to the study conception and design as well as methodology. M.S. did the formal analysis and investigation, as well as wrote the original manuscript. C.P. and A.M. edited the manuscript.

Code availability The Matlab codes used for solving the 2D partial differential equations for the bulk actomyosin network as well as the implementation of the IBM in 2D for a contractile viscoelastic fiber are available on Github https://github.com/mariyasavinov/ContractileStressFibers.git.

Declarations

Conflict of interest The authors declare that they have no conflict of interest.

References

Alexandrova AY, Arnold K, Schaub S, Vasiliev JM, Meister J-J, Bershadsky AD, Verkhovsky AB (2008) Comparative dynamics of retrograde actin flow and focal adhesions: formation of nascent adhesions triggers transition from fast to slow flow. PLoS ONE 3(9):3234. https://doi.org/10.1371/journal.pone.0003234

Bershadsky AD, Ballestrem C, Carramusa L, Zilberman Y, Gilquin B, Khochbin S, Alexandrova AY, Verkhovsky AB, Shemesh T, Kozlov MM (2006) Assembly and mechanosensory function of focal adhesions: experiments and models. Eur J Cell Biol 85(3):165–173. https://doi.org/10.1016/j.ejcb.2005.11.001

Blanchoin L, Boujemaa-Paterski R, Sykes C, Plastino J (2014) Actin dynamics, architecture, and mechanics in cell motility. Physiol Rev 94(1):235–263. https://doi.org/10.1152/physrev.00018.2013

Besser A, Colombelli J, Stelzer EHK, Schwarz US (2011) Viscoelastic response of contractile filament bundles. Phys Rev E 83(5):051902. https://doi.org/10.1103/PhysRevE.83.051902

Burridge K, Guilluy C (2016) Focal adhesions, stress fibers and mechanical tension. Exp Cell Res 343(1):14–20. https://doi.org/10.1016/j.yexcr.2015.10.029

Bischofs IB, Klein F, Lehnert D, Bastmeyer M, Schwarz US (2008) Filamentous network mechanics and active contractility determine cell and tissue shape. Biophys J 95(7):3488–3496. https://doi.org/10.1529/biophysj.108.134296

Brand CA, Linke M, Weißenbruch K, Richter B, Bastmeyer M, Schwarz US (2017) Tension and elasticity contribute to fibroblast cell shape in three dimensions. Biophys J 113(4):770–774. https://doi.org/10.1016/j.bpj.2017.06.058

Bringley TT, Peskin CS (2008) Validation of a simple method for representing spheres and slender bodies in an immersed boundary method for Stokes flow on an unbounded domain. J Comput Phys 227(11):5397–5425. https://doi.org/10.1016/j.jcp.2008.01.048

Brieher W (2013) Mechanisms of actin disassembly. Mol Biol Cell 24(15):2299–2302. https://doi.org/10.1091/mbc.E12-09-0694

Buenaventura A, Saito T, Kanao T, Matsunaga D, Matsui TS, Deguchi S (2024) Intracellular macromolecular crowding within individual stress fibers analyzed by fluorescence correlation spectroscopy. Cell Mol Bioeng 17(3):165–176. https://doi.org/10.1007/s12195-024-00803-4

Bernal R, Van Hemelryck M, Gurchenkov B, Cuvelier D (2022) Actin stress fibers response and adaptation under stretch. Int J Mol Sci 23(9):5095. https://doi.org/10.3390/ijms23095095

Cramer MS, Bahmani F (2014) Effect of large bulk viscosity on large-Reynolds-number flows. J Fluid Mech 751:142–163. https://doi.org/10.1017/jfm.2014.294

Colombelli J, Besser A, Kress H, Reynaud EG, Girard P, Caussinus E, Haselmann U, Small JV, Schwarz US, Stelzer EHK (2009) Mechanosensing in actin stress fibers revealed by a close correlation between force and protein localization. J Cell Sci 122(10):1665–1679. https://doi.org/10.1242/jcs.042986

Chapin LM, Edgar LT, Blankman E, Beckerle MC, Shiu YT (2014) Mathematical modeling of the dynamic mechanical behavior of neighboring sarcomeres in actin stress fibers. Cell Mol Bioeng 7(1):73–85. https://doi.org/10.1007/s12195-013-0318-3

Costa KD, Hucker WJ, Yin FC-P (2002) Buckling of actin stress fibers: a new wrinkle in the cytoskeletal tapestry. Cell Motil Cytoskelet 52(4):266–274. https://doi.org/10.1002/cm.10056

Cramer LP (1999) Organization and polarity of actin filament networks in cells: implications for the mechanism of myosin-based cell motility. Biochem Soc Symp 65:173–205

Cramer MS (2012) Numerical estimates for the bulk viscosity of ideal gases. Phys Fluids 24(6):066102. https://doi.org/10.1063/1.4729611

Cramer LP, Siebert M, Mitchison TJ (1997) Identification of novel graded polarity actin filament bundles in locomoting heart fibroblasts: implications for the generation of motile force. J Cell Biol 136(6):1287–1305. https://doi.org/10.1083/jcb.136.6.1287

Dillon R, Fauci L, Fogelson A, Gaver D III (1996) Modeling biofilm processes using the immersed boundary method. J Comput Phys 129(1):57–73. https://doi.org/10.1006/jcph.1996.0233

Fogelson B, Mogilner A (2018) Actin-myosin force generation and symmetry breaking in the model contractile fiber. SIAM J Appl Math 78(3):1754–1777. https://doi.org/10.1137/17M1112261

Fauci LJ, Peskin CS (1988) A computational model of aquatic animal locomotion. J Comput Phys 77(1):85–108. https://doi.org/10.1016/0021-9991(88)90158-1

Gavara N, Chadwick RS (2016) Relationship between cell stiffness and stress fiber amount, assessed by simultaneous atomic force microscopy and live-cell fluorescence imaging. Biomech Model Mechanobiol 15:511–523. https://doi.org/10.1007/s10237-015-0706-9

Heisenberg C-P, Bellaïche Y (2013) Forces in tissue morphogenesis and patterning. Cell 153(5):948–962. https://doi.org/10.1016/j.cell.2013.05.008

Hotulainen P, Lappalainen P (2006) Stress fibers are generated by two distinct actin assembly mechanisms in motile cells. J Cell Biol 173(3):383–394. https://doi.org/10.1083/jcb.200511093

Hamlet C, Santhanakrishnan A, Miller LA (2011) A numerical study of the effects of bell pulsation dynamics and oral arms on the exchange currents generated by the upside-down jellyfish *Cassiopea xamachana*. J Exp Biol 214(11):1911–1921. https://doi.org/10.1242/jeb.052506

Hayakawa K, Tatsumi H, Sokabe M (2008) Actin stress fibers transmit and focus force to activate mechanosensitive channels. J Cell Sci 121(4):496–503. https://doi.org/10.1242/jcs.022053

Isenberg G, Rathke PC, Hülsmann N, Franke WW, Wohlfarth-Bottermann KE (1976) Cytoplasmic actomyosin fibrils in tissue culture cells. Cell Tissue Res 166(4):427–443. https://doi.org/10.1007/BF00225909

Kreis TE, Birchmeier W (1980) Stress fiber sarcomeres of fibroblasts are contractile. Cell 22(2 Pt 2):555–561. https://doi.org/10.1016/0092-8674(80)90365-7

Kassianidou E, Brand CA, Schwarz US, Kumar S (2017) Geometry and network connectivity govern the mechanics of stress fibers. Proc Natl Acad Sci 114(10):2622–2627. https://doi.org/10.1073/pnas.1606649114

Kumar A, Graham MD (2015) Cell Distribution and Segregation Phenomena During Blood Flow. In: Spagnolie SE (ed) Complex fluids in biological systems: experiment, theory, and computation. Springer, New York, NY, pp 399–435. https://doi.org/10.1007/978-1-4939-2065-5_11

Kaunas R, Hsu H-J, Deguchi S (2010) Sarcomeric model of stretch-induced stress fiber reorganization. Cell Health Cytoskelet 3:13–22. https://doi.org/10.2147/CHC.S14984

Khatau SB, Hale CM, Stewart-Hutchinson PJ, Patel MS, Stewart CL, Searson PC, Hodzic D, Wirtz D (2009) A perinuclear actin cap regulates nuclear shape. Proc Natl Acad Sci 106(45):19017–19022. https://doi.org/10.1073/pnas.0908686106

Kumar S, Maxwell IZ, Heisterkamp A, Polte TR, Lele TP, Salanga M, Mazur E, Ingber DE (2006) Viscoelastic retraction of single living stress fibers and its impact on cell shape, cytoskeletal organization, and extracellular matrix mechanics. Biophys J 90(10):3762–3773. https://doi.org/10.1529/biophysj.105.071506

Keller JB, Rubinow SI (1976) Slender-body theory for slow viscous flow. J Fluid Mech 75(4):705–714. https://doi.org/10.1017/S0022112076000475

Linsmeier I, Banerjee S, Oakes PW, Jung W, Kim T, Murrell MP (2016) Disordered actomyosin networks are sufficient to produce cooperative and telescopic contractility. Nat Commun 7(1):12615. https://doi.org/10.1038/ncomms12615

Livne A, Geiger B (2016) The inner workings of stress fibers-from contractile machinery to focal adhesions and back. J Cell Sci 129(7):1293–1304. https://doi.org/10.1242/jcs.180927

Lewis OL, Guy RD, Allard JF (2014) Actin-myosin spatial patterns from a simplified isotropic viscoelastic model. Biophys J 107(4):863–870. https://doi.org/10.1016/j.bpj.2014.06.041

Le Goff T, Liebchen B, Marenduzzo D (2020) Actomyosin contraction induces in-bulk motility of cells and droplets. Biophys J 119(5):1025–1032. https://doi.org/10.1016/j.bpj.2020.06.029

Lee S, Kassianidou E, Kumar S (2018) Actomyosin stress fiber subtypes have unique viscoelastic properties and roles in tension generation. Mol Biol Cell 29(16):1992–2004. https://doi.org/10.1091/mbc.E18-02-0106

Lee W, Lim S, Kim Y (2017) The role of myosin II in glioma invasion: a mathematical model. PLoS ONE 12(2):0171312. https://doi.org/10.1371/journal.pone.0171312

Lu L, Oswald SJ, Ngu H, Yin FC-P (2008) Mechanical properties of actin stress fibers in living cells. Biophys J 95(12):6060–6071. https://doi.org/10.1529/biophysj.108.133462

Lehtimäki JI, Rajakylä EK, Tojkander S, Lappalainen P (2021) Generation of stress fibers through myosin-driven reorganization of the actin cortex. Elife 10:60710. https://doi.org/10.7554/eLife.60710

Mayer M, Depken M, Bois JS, Jülicher F, Grill SW (2010) Anisotropies in cortical tension reveal the physical basis of polarizing cortical flows. Nature 467(7315):617–621. https://doi.org/10.1038/nature09376

Maxian O, Donev A, Mogilner A (2022) Interplay between Brownian motion and cross-linking controls bundling dynamics in actin networks. Biophys J 121(7):1230–1245. https://doi.org/10.1016/j.bpj.2022.02.030

Malik-Garbi M, Ierushalmi N, Jansen S, Abu-Shah E, Goode BL, Mogilner A, Keren K (2019) Scaling behaviour in steady-state contracting actomyosin networks. Nat Phys 15(5):509–516. https://doi.org/10.1038/s41567-018-0413-4

Mogilner A, Manhart A (2018) Intracellular fluid mechanics: coupling cytoplasmic flow with active cytoskeletal gel. Ann Rev Fluid Mech 50:347–370. https://doi.org/10.1146/annurev-fluid-010816-060238. (**2018**)

Maxian O, Peskin CS (2020) An immersed boundary method with subgrid resolution and improved numerical stability applied to slender bodies in stokes flow. SIAM J Sci Comput 42(4):847–868. https://doi.org/10.1137/19M1280879

Maxian O, Peláez RP, Mogilner A, Donev A (2021) Simulations of dynamically cross-linked actin networks: morphology, rheology, and hydrodynamic interactions. PLoS Comput Biol 17(12):1009240. https://doi.org/10.1371/journal.pcbi.1009240

Nazockdast E, Rahimian A, Zorin D, Shelley M (2017) A fast platform for simulating semi-flexible fiber suspensions applied to cell mechanics. J Comput Phys 329:173–209. https://doi.org/10.1016/j.jcp.2016.10.026

Oakes PW, Banerjee S, Marchetti MC, Gardel ML (2014) Geometry regulates traction stresses in adherent cells. Biophys J 107(4):825–833. https://doi.org/10.1016/j.bpj.2014.06.045

Peskin CS (1972) Flow patterns around heart valves: a numerical method. J Comput Phys 10(2):252–271. https://doi.org/10.1016/0021-9991(72)90065-4

Peskin CS (2002) The immersed boundary method. Acta Numer 11:479–517. https://doi.org/10.1017/S0962492902000077

Park Y, Kim Y, Lim S (2019) Flagellated bacteria swim in circles near a rigid wall. Phys Rev E 100(6):063112. https://doi.org/10.1103/PhysRevE.100.063112

Pellegrin S, Mellor H (2007) Actin stress fibres. J Cell Sci 120(20):3491–3499. https://doi.org/10.1242/jcs.018473

Peterson LJ, Rajfur Z, Maddox AS, Freel CD, Chen Y, Edlund M, Otey C, Burridge K (2004) Simultaneous stretching and contraction of stress fibers in vivo. Mol Biol Cell 15(7):3497–3508. https://doi.org/10.1091/mbc.e03-09-0696

Rubinstein B, Fournier MF, Jacobson K, Verkhovsky AB, Mogilner A (2009) Actin-myosin viscoelastic flow in the keratocyte Lamellipod. Biophys J 97(7):1853–1863. https://doi.org/10.1016/j.bpj.2009.07.020

Rid R, Schiefermeier N, Grigoriev I, Small JV, Kaverina I (2005) The last but not the least: the origin and significance of trailing adhesions in fibroblastic cells. Cell Motil Cytoskelet 61(3):161–171. https://doi.org/10.1002/cm.20076

Rutkowski DM, Vavylonis D (2021) Discrete mechanical model of lamellipodial actin network implements molecular clutch mechanism and generates arcs and microspikes. PLoS Comput Biol 17(10):1009506. https://doi.org/10.1371/journal.pcbi.1009506

Riedel L, Wössner V, Kempf D, Ziebert F, Bastian P, Schwarz US (2024) The positioning of stress fibers in contractile cells minimizes internal mechanical stress. arXiv. arXiv:2407.07797 [cond-mat, physics:physics, q-bio]. https://doi.org/10.48550/arXiv.2407.07797

Ruppel A, Wörthmüller D, Misiak V, Kelkar M, Wang I, Moreau P, Méry A, Révilloud J, Charras G, Cappello G, Boudou T, Schwarz US, Balland M (2023) Force propagation between epithelial cells depends on active coupling and mechano-structural polarization. eLife 12:83588. https://doi.org/10.7554/eLife.83588

Russell RJ, Xia S-L, Dickinson RB, Lele TP (2009) Sarcomere mechanics in capillary endothelial cells. Biophys J 97(6):1578–1585. https://doi.org/10.1016/j.bpj.2009.07.017

Sherrard KM, Cetera M, Horne-Badovinac S (2021) DAAM mediates the assembly of long-lived, treadmilling stress fibers in collectively migrating epithelial cells in *Drosophila*. eLife 10:72881. https://doi.org/10.7554/eLife.72881

Strychalski W, Copos CA, Lewis OL, Guy RD (2015) A poroelastic immersed boundary method with applications to cell biology. J Comput Phys 282:77–97. https://doi.org/10.1016/j.jcp.2014.10.004

Schakenraad K, Ernst J, Pomp W, J. Danen E.H, H. Merks R.M, Schmidt T, Giomi L (2020) Mechanical interplay between cell shape and actin cytoskeleton organization. Soft Matter 16(27):6328–6343. https://doi.org/10.1039/D0SM00492H

Strychalski W, Guy RD (2012) Viscoelastic immersed boundary methods for zero Reynolds number flow. Commun Comput Phys 12(2):462–478. https://doi.org/10.4208/cicp.050211.090811s

Strychalski W, Guy RD (2013) A computational model of bleb formation. Math Med Biol J IMA 30(2):115–130. https://doi.org/10.1093/imammb/dqr030

Schmoller KM, Lieleg O, Bausch AR (2009) Structural and viscoelastic properties of actin/filamin networks: cross-linked versus bundled networks. Biophys J 97(1):83–89. https://doi.org/10.1016/j.bpj.2009.04.040

Sato M, Ohashi T (2005) Biorheological views of endothelial cell responses to mechanical stimuli. Biorheology 42(6):421–441

Stachowiak MR, O'Shaughnessy B (2009) Recoil after severing reveals stress fiber contraction mechanisms. Biophys J 97(2):462–471. https://doi.org/10.1016/j.bpj.2009.04.051

Saintillan D, Shelley MJ (2015) Theory of active suspensions. In: Spagnolie SE (ed) Complex fluids in biological systems: experiment, theory, and computation. Springer, New York, NY, pp 319–355. https://doi.org/10.1007/978-1-4939-2065-5_9

Tanner K, Boudreau A, Bissell MJ, Kumar S (2010) Dissecting regional variations in stress fiber mechanics in living cells with laser nanosurgery. Biophys J 99(9):2775–2783. https://doi.org/10.1016/j.bpj.2010.08.071

Tojkander S, Gateva G, Lappalainen P (2012) Actin stress fibers–assembly, dynamics and biological roles. J Cell Sci. https://doi.org/10.1242/jcs.098087

Tojkander S, Gateva G, Schevzov G, Hotulainen P, Naumanen P, Martin C, Gunning PW, Lappalainen P (2011) A molecular pathway for myosin II recruitment to stress fibers. Current Biol CB 21(7):539–550. https://doi.org/10.1016/j.cub.2011.03.007

Tytell ED, Hsu C-Y, Williams TL, Cohen AH, Fauci LJ (2010) Interactions between internal forces, body stiffness, and fluid environment in a neuromechanical model of lamprey swimming. Proc Natl Acad Sci 107(46):19832–19837. https://doi.org/10.1073/pnas.1011564107

Trichet L, Le Digabel J, Hawkins RJ, Vedula SRK, Gupta M, Ribrault C, Hersen P, Voituriez R, Ladoux B (2012) Evidence of a large-scale mechanosensing mechanism for cellular adaptation to substrate stiffness. Proc Natl Acad Sci 109(18):6933–6938. https://doi.org/10.1073/pnas.1117810109

Tornberg A-K, Shelley MJ (2004) Simulating the dynamics and interactions of flexible fibers in Stokes flows. J Comput Phys 196(1):8–40. https://doi.org/10.1016/j.jcp.2003.10.017

Vignaud T, Copos C, Leterrier C, Toro-Nahuelpan M, Tseng Q, Mahamid J, Blanchoin L, Mogilner A, Théry M, Kurzawa L (2021) Stress fibres are embedded in a contractile cortical network. Nat Mater 20(3):410–420. https://doi.org/10.1038/s41563-020-00825-z

Vavylonis D, Wu J.-Q, Hao S, O'Shaughnessy B, Pollard TD (2008) Assembly mechanism of the contractile ring for cytokinesis by fission yeast. Science 319(5859):97–100. https://doi.org/10.1126/science.1151086

Yan W, Ansari S, Lamson A, Glaser MA, Blackwell R, Betterton MD, Shelley M (2022) Toward the cellular-scale simulation of motor-driven cytoskeletal assemblies. Elife 11:74160. https://doi.org/10.7554/eLife.74160

Zand MS, Albrecht-Buehler G (1989) What structures, besides adhesions, prevent spread cells from rounding up? Cell Motil Cytoskelet 13(3):195–211. https://doi.org/10.1002/cm.970130307

Supplement for *A model for contractile stress fibers embedded in bulk actomyosin networks*

Mariya Savinov [1*], Charles S. Peskin [1] and Alex Mogilner [1,2*]

[1*]Courant Institute of Mathematical Sciences, New York University.
[2]Department of Biology, New York University.

*Corresponding author(s). E-mail(s): mas10009@nyu.edu;
mogilner@cims.nyu.edu;
Contributing authors: peskin@cims.nyu.edu;

1 Scaling and non-dimensionalization for stress fiber model

We nondimensionalize the stress fiber (SF) forces using the same scales introduced in main text Sec. 2.1, summarized here in Table S1. For the fiber, both the reference

Table S1 Scales for non-dimensionalization

Spatial	Velocity	Myosin	Timescale	Fiber Force
R	$\frac{Mm_0}{\zeta R}$	m_0	$\frac{\zeta R^2}{Mm_0}$	$f_0 = Mm_0R$

configuration q and current configuration $\boldsymbol{X}$ are scaled by R, so it remains to determine the non-dimensional analogues of fiber parameters K_E, K_B, ξ, F_s, v_0, and k_{adh}.

For the elastic force (12), we can nondimensionalize the elastic modulus K_E by the $f_0 = Mm_0R$ force scale to get the non-dimensional tension:

$$T = \frac{K_E}{f_0}\left(\left\|\frac{\partial \boldsymbol{X}}{\partial q}\right\| - 1\right) \longrightarrow K_E\left(\left\|\frac{\partial \boldsymbol{X}}{\partial q}\right\| - 1\right) . \tag{S1}$$

Note that $\partial \boldsymbol{X}/\partial q$ is equivalent to its nondimensional counterpart. Similarly, the tangent vector is without dimensions, so applying the above tension to (12) yields the non-dimensionalized elastic force density

$$\boldsymbol{F}^e(q) = -\frac{\delta E_e}{\delta \boldsymbol{X}} = \frac{1}{R}\frac{\partial}{\partial q}\left(T\boldsymbol{\tau}\right) \ . \tag{S2}$$

Note that for the numerical implementation, we will consider forces as opposed to force densities, so the $1/R$ factor will be dropped.

For the bending force (14), we nondimensionalize the bending modulus K_B using the force scale f_0 and spatial scale R to get the nondimensional bending force density

$$\boldsymbol{F}^b(q) = -\frac{1}{R}\frac{K_B}{f_0 R^2}\frac{\partial^4 \boldsymbol{X}}{\partial q^4} \longrightarrow -\frac{1}{R}K_B\frac{\partial^4 \boldsymbol{X}}{\partial q^4} \ . \tag{S3}$$

Similar to the elastic force density (S2), we rescale $K_B/f_0R^2 \to K_B$ and the additional $1/R$ factor above will be dropped.

The viscous force (15) is straightforward to nondimensionalize by utilizing the scale for time $\zeta R^2/Mm_0$ and force f_0 as follows:

$$\boldsymbol{F}^v = \frac{\xi}{f_0}\frac{Mm_0}{\zeta R^2}\frac{\partial}{\partial t}\left\|\frac{\partial \boldsymbol{X}}{\partial q}\right\|\boldsymbol{\tau} = \frac{\xi}{\zeta R^3}\frac{\partial}{\partial t}\left\|\frac{\partial \boldsymbol{X}}{\partial q}\right\|\boldsymbol{\tau} \longrightarrow \xi\frac{\partial}{\partial t}\left\|\frac{\partial \boldsymbol{X}}{\partial q}\right\|\boldsymbol{\tau} \ . \tag{S4}$$

Note that here we have a nondimensional force, not force density, so we rescale $\xi/\zeta R^3 \to \xi$.

For the myosin force (16), it is straightforward to nondimensionalize the fiber force $F_s \to F_S/f_0$ and the free velocity per unit length $v_0\, Mm_0/\zeta R^2 \to v_0$:

$$F^m = \frac{F_s}{f_0}\left(1 + \frac{1}{v_0 Mm_0 L_0/\zeta R^2}\frac{dL}{dt}\right) \to F_s\left(1 + \frac{1}{v_0 L_0}\frac{dL}{dt}\right) \ . \tag{S5}$$

Finally, for the adhesion forces, we nondimensionalize the spring constant as $k_{adh}R/f_0 \to k_{adh}$. If the adhesions are uniformly distributed along the length of the fiber, instead nondimensionalize $k_{adh}/f_0 \to k_{adh}$.

Table S2 summarizes the system parameters, both for the actomyosin network and SF, as well as their dimensional values used for simulations and non-dimensional counterparts.

Table S2 Parameters, their dimensional values for simulations (Figs. 7, 8, S4, S5), non-dimensional analogues, and references for scales. Note we consider a legthscale of cell size $R = 50\,\mu$m.

Parameter		Value	Non-dim	References and Notes
Actin network viscosity (2D)	μ	$400\,\text{pN}\cdot\text{s}/\mu\text{m}$	$\mu/\zeta R^2$	Following (Rubinstein et al., 2009): actin network viscosity in 3D is $\sim 2\,$kPa·s (Bausch et al., 1998) and assuming a network thickness of $\sim 0.2\,\mu$m, comparable to fibroblast lamellipod (Abraham et al., 1999)
Network expansion viscosity	λ	$400\,\text{pN}\cdot\text{s}/\mu\text{m}$	$\lambda/\zeta R^2$	On scale comparable to μ. For example, for water $\lambda = 3\mu$ (Cramer, 2012)
Actin network drag coefficient	ζ	$0.25\,\text{pN}\cdot\text{s}/\mu\text{m}^3$	1	If the result of adhesive forces, could be as large as $1000\,\text{pN}\cdot\text{s}/\mu\text{m}^3$ (Rubinstein et al., 2009) If the result of Darcy friction with the cytosol, could be as small as $O(0.1\,\text{pN}\cdot s/\mu\text{m}^3)$, an order of magnitude smaller than contractile and viscous forces (Malik-Garbi et al., 2019).
Myosin contractile stress	Mm_0	$20\,\text{pN}/\mu\text{m}$	1	Following (Rubinstein et al., 2009): characteristic myosin contractile stress in 3D is $\sim 100\,\text{pN}/\mu\text{m}^3$ (Oliver et al., 1999; Galbraith and Sheetz, 1999). Assuming a thickness of $\sim 0.2\mu m$ such as for fibroblast lamellipod (Abraham et al., 1999).
Myosin diffusion coefficient	d_0	$0.15\,\mu\text{m}^2/\text{s}$	$d_0\zeta/Mm_0$	Comparable to the experimentally measured value of $0.8\,\mu\text{m}^2/\text{s}$ (Uehara et al., 2010). In a model for myosin dynamics, Luo et al. (2012) use a similar value of $0.2\,\mu\text{m}^2/\text{s}$.
Myosin detachment rate	α	$0.018/\text{s}$	$\alpha\zeta R^2/Mm_0$	Not measured, but Rubinstein et al. (2009) used a similar model for myosin in migrating cells and needed $\alpha < 0.01$ to replicate experimental conditions.
Myosin attachment rate	β	$0.018/\text{s}$	$\beta\zeta R^2/Mm_0$	Not measured, but assumed comparable to the attachment rate α.
Elastic fiber force coefficient	K_E	$250\,\text{pN}$	K_E/Mm_0R	Lu et al. (2008) report a SF stiffness of $\sim 10\,\text{pN}/\mu\text{m}^2$, used in other studies such as (Riedel et al., 2024). Using SF widths $\sim 1\,\mu$m, this yields $K_E \sim 10$pN. On the other hand, Kassianidou et al. (2017) consider SF stiffness on the scale of 5 nN. Generally there is wide variability in stress fiber stiffness measurements (Livne and Geiger, 2016), so we choose a parameter value between these divergent orders of magnitude.
Bending fiber force coefficient	K_B	$2500\,\text{pN}\cdot\mu\text{m}^2$	K_B/Mm_0R^3	Single actin filaments have a persistence length of $17\,\mu$m (Gittes et al., 1993) and thus bending stiffness of $0.07\,\text{pN}\cdot\mu\text{m}^2$. Stiffness of heavily crosslinked actin bundles such as in SFs scales like the number of cross-linked filaments squared (Mogilner and Rubinstein, 2005), so we choose a K_B for a thick SF corresponding to $\sim$ 100-many crosslinked filaments.
Fiber internal viscosity	ξ	$1000\,\text{pN}\cdot\text{s}$	$\xi/\zeta R^3$	Isolated stress fibers were measured to have a mean viscosity of $7850\,\text{pN}\cdot s/\mu$m (Labouesse et al., 2016). Our viscosity coefficient per unit length is an order of magnitude smaller in part due to computational limitations.
Myosin stall force	F_s	$50\,\text{pN}$	F/Mm_0R	Investigating forces on focal adhesions, Schwarz et al. (2006) consider $F_s \sim 1\,$pN, on the scale of forces generated by single motors (Livne and Geiger, 2016). However, contractile forces in SF are measured to be as large as on $\sim 1\,$nN (Livne and Geiger, 2016; Kassianidou et al., 2017), though this contradicts expected SF rest lengths (Livne and Geiger, 2016). We choose a contractile force within the range of possible active forces, depending on myosin distribution within the SF.
Myosin free velocity	v_0	$0.5/\text{s}$	$v_0\zeta R^2/Mm_0$	The free velocity of myosin motors is between $\sim 1\,\mu$m/s and $\sim 10\,\mu$m/s (Schwarz et al., 2006; Schwarz and Safran, 2013), which is $\sim 0.1/$s to $\sim 1/$s per unit length for stress fibers $\sim 10\,\mu$m long, as we consider.
Adhesion spring coefficient	k_{adh}	$2000\,\text{pN}/\mu\text{m}$	k_{adh}/Mm_0	Focal adhesion spring constants can range from $\sim 1\,\text{pN}/\mu\text{m}$ to $\sim 1\,$pN/nm, depending on the bulk modulus of the underlying material (Schwarz et al., 2006). Moreover, stiffness of complex protein bindings can range as large as $\sim 10\,$pN/nm (Kaya and Higuchi, 2010), so we choose an intermediate stiffness.

2 Supplemental figure details and movie captions

2.1 Additional main text figure details

For Fig. 2-Fig. 8, we note here additional details relating to grid sizes, timestep size, and calculations of timescales:

- Fig. 2: All solutions are computed on a 128×128 Eulerian grid.
- Fig. 3: The steady state distributions are computed by numerically solving the system on a 128×128 grid with timestep $\Delta t = 0.001$ until the relative L_∞ norm of the myosin distribution over 0.2 time units varies by less than 10^{-4}. There are minimal quantitative differences if a smaller grid-size and timestep are used.
- Fig. 4: **(a)** The numerical solution was computed with a $\Delta t = 0.0001$ timestep and $N_b = 60$ Lagrangian points. **(b)** The timescales were calculated by numerically solving for the fiber configurations over a $T = 1.0$ time with a $\Delta t = 0.0001$ timestep and $N_b = 60$ Lagrangian points. The length over time was then fit to an exponential using `MATLAB`'s `fit` function. **(c)** The configuration was solved numerically with a $\Delta t = 0.000001$ timestep and $N_b = 60$ Lagrangian points. **(d)** The timescales were calculated by numerically solving for the fiber configurations over a $T = 0.8$ time with a $\Delta t = 0.000001$ timestep and $N_b = 60$ Lagrangian points. The maximum curvature over time was then fit to an exponential using `MATLAB`'s `fit` function.
- Fig. 5: The timescales, velocity, and configuration profiles were calculated by numerically solving for the fiber configurations over a $T = 3.0$ time with a $\Delta t = 0.001$ timestep, $N_b = 60$ Lagrangian points, and on a 100×100 actin network Eulerian grid. The length over time was then fit to an exponential using `MATLAB`'s `fit` function.
- Fig. 6: The timescales and profiles were calculated by numerically solving for the fiber configurations over a $T = 5.0$ time with a $\Delta t = 0.00005$ timestep, $N_b = 60$ Lagrangian points, and on a 100×100 actin network Eulerian grid. Note that omitted combinations of μ and K_B in **(a)** are those that require a smaller timestep for stability. The maximum curvature of the configuration over time was then fit to an exponential using `MATLAB`'s `fit` function.
- Fig. 7 and Fig. 8: The solution is computed over $T = 50.0$ time units with a $\Delta t = 0.001$ timestep, $N_b = 64$ Lagrangian points, and on a 128×128 actomyosin network Eulerian grid.

2.2 Movie 1 and Movie 2 captions

Movie 1

A timelapse of the numerical solution in Fig. 7 over time for the case of four stress fibers with adhesions at their ends immersed in a bulk actomyosin network with initial bound and free myosin distributions as shown in the top row of main text Fig. 3(b). The stress fibers have an elastic modulus $K_E = 0.25$, bending modulus $K_B = 0.001$, internal viscosity $\xi = 0.035$, contractile stall force $F_s = 0.05$, and contractile free velocity $v_0 = 15$. The end adhesions have a spring force of $k_{adh} = 100$. The quiver scale is such that a speed of 1 scales to 3 spatial units. The solution is computed over $T = 50.0$ time with a $\Delta t = 0.001$ timestep, $N_b = 64$ Lagrangian points, and on a 128×128 actomyosin network Eulerian grid.

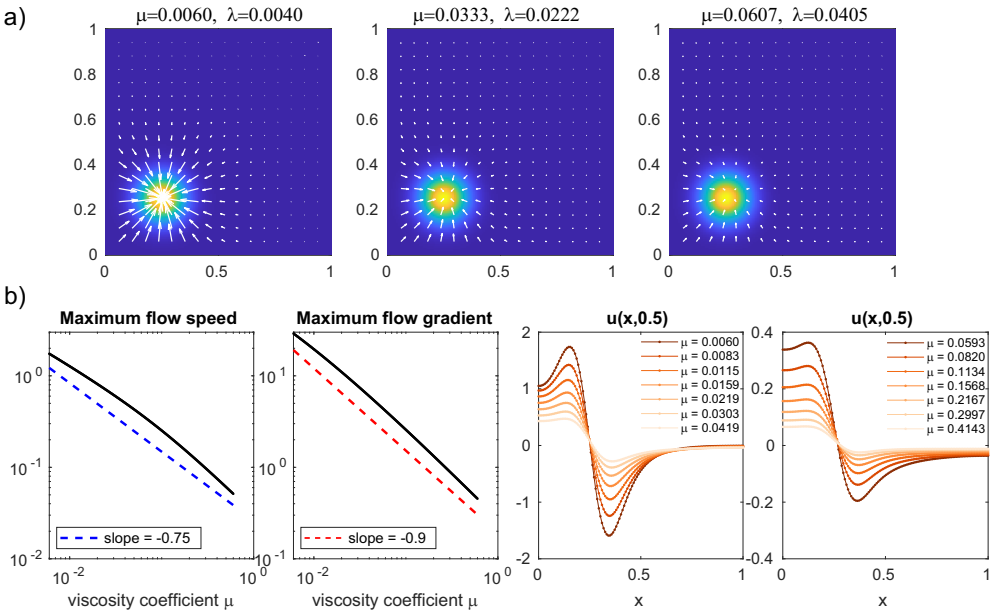

Fig. S1 **(a)** Numerical solutions on a 128×128 Eulerian grid for the flow of the actomyosin network for different network viscosities in the case of a gaussian-like distribution of bound myosin (24) in the corner $(x_0, y_0) = (0.25, 0.25)$ of the domain $\Omega = [0,1] \times [0,1]$. The first viscosity coefficient μ is varied and the expansion viscosity $\lambda = 2\mu/3$ in all cases. The flow quiver arrows are identically scaled between all subplots, such that a flow speed of 1 appears as an arrow of size 0.07 in the domain. **(b)** Quantitative differences in flow properties around the myosin distribution in (a) as a function of changing actin network first viscosity coefficient μ with expansion viscosity $\lambda = 2\mu/3$, as computed on a 128×128 Eulerian grid. The left two columns show the maximum flow speeds and gradients, respectively, as a function of increasing viscosity on a log-log plot. The right two columns show the flow distribution along the horizontal midline of the myosin peak as a function of horizontal position x for a few cases of μ, ranging from $\mu = 0.006$ to $\mu = 0.4143$, with lighter colors corresponding to larger values of μ.

Movie 2

A timelapse of the numerical solution in Fig. 8 over time starting at time $t = 25$, shortly before ablation at time $t = 30$, ending at time $t = 50.0$ continuing the conditions of Movie 1. The quiver scale is such that a speed of 1 scales to 3 spatial units.

3 Bulk actomyosin network dynamics

3.1 Off-center myosin spot

If myosin is concentrated near the corner of the domain, Fig. S1 shows that the maximal induced flow gradient is similar to when myosin is concentrated in the center (Fig 2), decreasing like $1/\mu^{0.9}$. However, we see that the maximum flow speed decreases more slowly with μ when myosin is concentrated close to the boundary, approximately $1/\mu^{0.75}$. This can be explained by looking at the horizontal flow at $y = 0.25$: the no-stress boundary condition results in faster flow of the actin network which is on the left

$(0 < x < 0.25)$ than on the the right $(0.25 < x < 1)$. We can explain this physically as follows: there is less actin network for the myosin to pull to the left $(0 < x < 0.25)$ than to the right $(0.25 < x < 1.0)$. The total drag on the left part of the network is smaller than the drag on the right part of the network, so the left part contracts toward the myosin spot faster. Experiments have shown how myosin spots contract corners and edges of actin networks first (Colin et al., 2023), and this agrees with those results.

3.2 Varying expansion viscosity λ

For viscous fluids, the expansion viscosity could in principle be as large as an order or two magnitude larger than the first viscosity coefficient. Meanwhile for fluids like water, the first viscosity and expansion viscosity are on the same order of magnitude (Cramer, 2012). Consider fixing μ and changing λ: Fig. S2 shows the maximum flow speed, maximum flow gradient, and sample flow profiles for the cases of $\mu = 0.006$ and $\mu = 0.06$. Unlike varying μ and λ together, the change in the flow speed and gradient

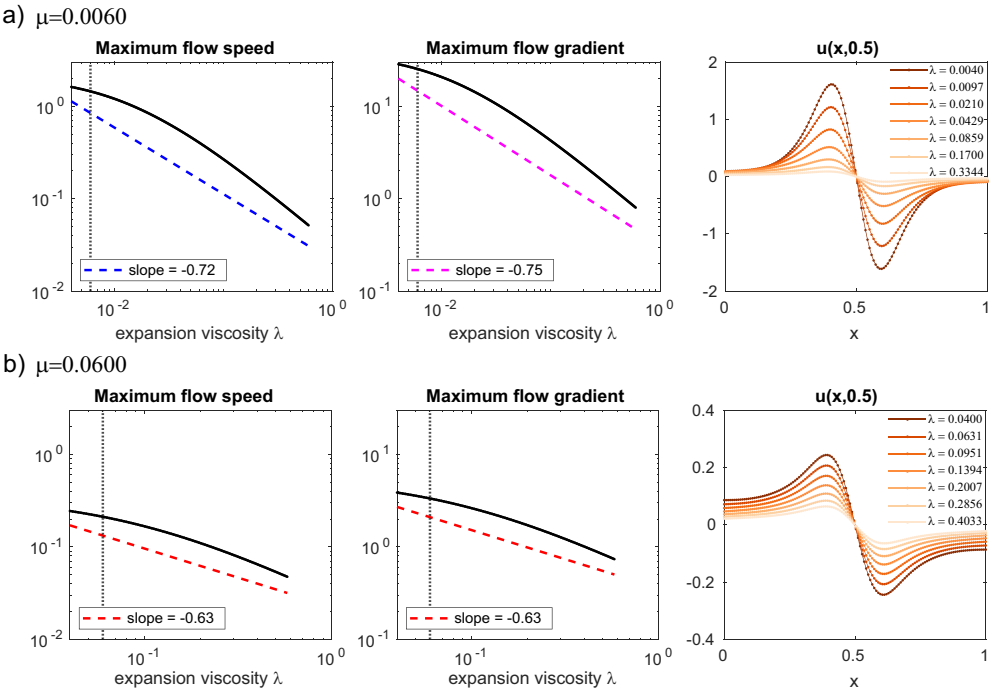

Fig. S2 Quantitative difference in flow properties around the myosin distribution shown in main text Fig. 2(a) as a function of varying bulk actin network viscosity λ for fixed choices of $\mu = 0.006$ (top) and $\mu = 0.06$ (bottom), as computed on a 128×128 Eulerian grid. The left and middle columns show the maximum flow speeds and gradients, respectively, as a function of increasing expansion viscosity on a log-log plot. The right column shows the flow distribution along the horizontal midline of the myosin peak as a function of horizontal position x for a few cases of λ, starting from $\lambda = 2\mu/3$, with lighter colors corresponding to larger values of λ.

does not vary like $1/\lambda^p$ for some $p < 1$. Similarly to increasing μ, however, increasing the expansion viscosity λ results in slower flows, as the actin network is more resistant to the compaction the contractile forces of the myosin spot are driving. Comparing Fig. 2 to plots in Fig. S2, we see that changing λ does not result in qualitatively different flow profiles than changing μ and λ together, aside from exact relation of maximum flow speed to λ.

4 Contracting fiber centered in the bulk network

The relations between K_E or μ with τ_L shown in main text Fig. 5 are conserved if the fiber is positioned differently in the bulk network. Fig. S3(a) shows the same timescale relations for a fiber placed symmetrically in the center of the domain – the only difference being that contraction is slightly faster, as the fiber does not have to compete with stretching flows resulting from contracting near the bulk network boundary. Fig. 5(c-e) shows how fiber placement near the boundary results in bulk network flow perpendicular to the fiber axis, and these flows stretch the fiber, contrary to the contractile action of the myosin along the fiber length, inevitably increasing the contraction timescale due to competing processes. Fibers which have lower elastic moduli K_E become bent as a result Fig. 5(c), while fibers that are stiffer along their length finish contracting before being hugely impacted Fig. 5(e). Meanwhile, a SF in the center of the domain contracts along its axis, and the flows perpendicular to its axis are outward, as seen in Fig. S3, so that the SF ultimately remains straight. If the fibers additionally resisted bending, then the length contraction and bending resistance timescales would be in competition, modifying the degree to which a fiber would be bent by the contractile flows seem in Fig. 5(c).

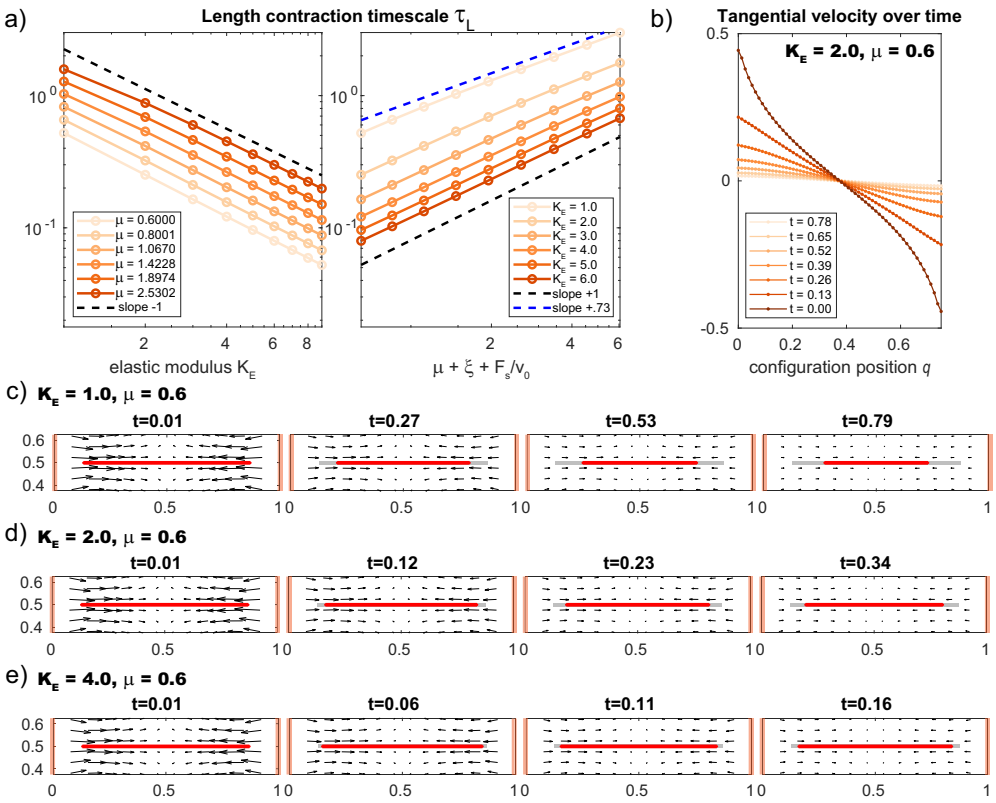

Fig. S3 **(a)** The numerically calculated timescales of length contraction τ_L for a contracting viscoelastic fiber immersed in a bulk actin network for variable elastic modulus K_E (left) and variable bulk network viscosity μ, $\lambda = 2\mu/3$ (right). The fiber is initialized at rest length 0.75 at the center of the domain from $x = 0.125$ to $x = 0.875$ with fixed contraction parameters $F_s = 0.5$ and $v_0 = 15$ and internal viscosity coefficient $\xi = 0.018$, largest value for which FPI converges for all shown parameter sets. The timescales and subsequent velocity and configuration profiles in (b-e) were calculated by numerically solving for the fiber configurations over a $T = 3.0$ time with a $\Delta t = 0.001$ timestep, $N_b = 60$ Lagrangian points, and on a 100×100 actin network Eulerian grid. **(b)** The tangential velocity of a contracting fiber over time for the case of $K_E = 2.0$ and a fluid viscosity of $\mu = 0.6$. **(c-e)** The configuration of a contracting fiber over time with elastic moduli $K_E = 1.0$, 2.0, 4.0, immersed in a bulk actin network with viscosity $\mu = 0.6$ with the corresponding flow shown in black arrows. The quiver scale is such that a speed of 1 scales to 0.35 spatial units. Thick light orange lines mark the boundaries of the domain.

5 Capturing *in vivo* leading edge flows

The 2D model is particularly applicable to experimental contexts where SFs are immersed in thin actomyosin bulk networks, such as those found in cells spread on flat surfaces (Rubinstein et al., 2009; Ruppel et al., 2023). Using the 2D model, we can for example explore the impact of SFs and their focal adhesions on retrograde actin flow in the leading edge of spread cells. In various cell types, Alexandrova et al.

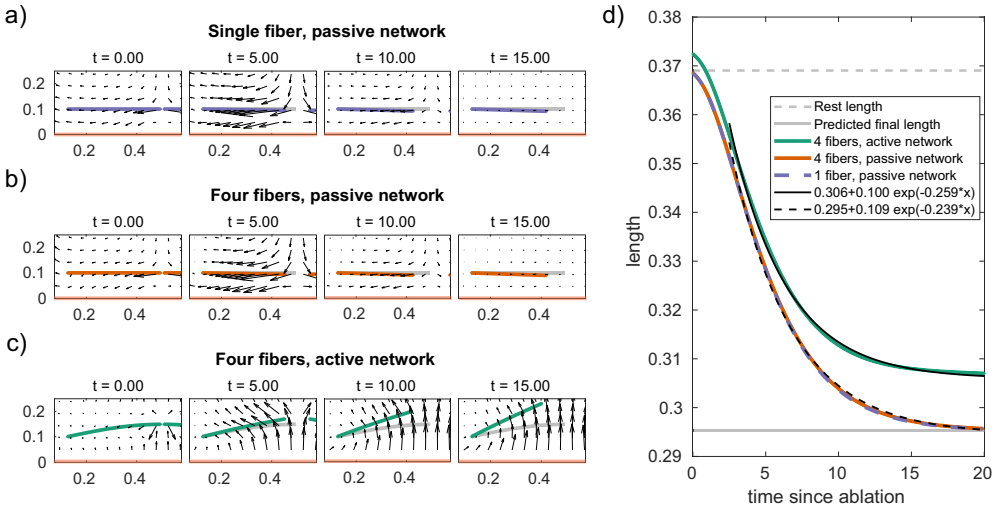

Fig. S4 The numerical solutions over time for a fiber after laser ablation, in the case of **(a)** a single fiber in a passive network, **(b)** four fibers in a passive network, and **(c)** four fibers in an active network. The length of the ablated fiber piece over time in all three cases is shown in **(d)**, along with exponential fits for the length change after time $T = 2.5$. The stress fibers have an elastic modulus $K_E = 0.25$, bending modulus $K_B = 0.001$, internal viscosity $\xi = 0.035$, contractile stall force $F_s = 0.05$, and contractile free velocity $v_0 = 15$. The end adhesions have a spring force of $k_{adh} = 100$. In **(a)** and **(b)**, the quiver scale is such that a speed of 1 scales to 20 spatial units. In **(c)**, the quiver scale is such that a speed of 1 scales to 10 spatial units. Thick light orange lines mark the boundaries of the domain. The solution is computed over $T = 20.0$ time units with a $\Delta t = 0.001$ timestep, $N_b = 64$ Lagrangian points, and on a 128×128 actomyosin network Eulerian grid.

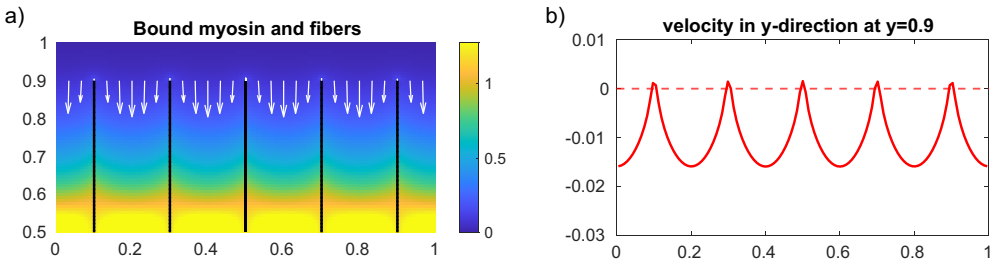

Fig. S5 The numerical solution for five SFs immersed in an active network which has periodic boundary conditions at $x = 0$ and $x = 1$ and no-stress conditions at $y = 0$ and $y = 1$. The stress fibers are viscoelastic and contractile with focal adhesions at their ends at $y = 0.1$ and $y = 0.9$, with the same parameters as in Fig. 7 and Fig. S4. **(a)** The bound myosin distribution and stress fiber positions (black lines) in the upper half of the domain, due to the mirror symmetry of the problem in the y direction. White quiver arrows represent the flow vectors of the network at $y = 0.9$, with a quiver scale such that a speed of 1 scales to 6 spatial units. **(b)** The y-component of the network flow field at $y = 0.9$ for the snapshot in (a). The solution is computed over $T = 2.0$ time units with a $\Delta t = 0.001$ timestep, $N_b = 64$ Lagrangian points, and on a 128×128 actomyosin network Eulerian grid. The bound and free myosin distributions are initialized as $m(x, y) = b(x, y) = \sin(\pi y)^2$.

(2008) observed that focal adhesions of stress fibers serve to partially block lamellipodial flow at the leading edge, effectively making the retrograde flow maximal in the middle between SFs and minimal close to SF ends. We can replicate the state of the network and SFs by employing our actomyosin bulk network model on a domain $R \times R = 50\mu m \times 50\mu m$ which is periodic in x, with x being a coarse representation of position along the leading edge (omitting angular contributions, assuming the cell is sufficiently large). We choose our conditions to be symmetric in y, such that $y = 0$ and $y = 1$ define opposite leading edges, and henceforth will focus on dynamics near the leading edge defined by $y = 1$. Utilizing SF distributions observed in (Alexandrova et al., 2008), we consider five SFs which are viscoelastic and contractile of length $40\mu m = 0.8R$, equally spaced $10\mu m$ apart, with their ends and focal adhesions $5\mu m$ away from the leading edge. As retrograde flow is driven by contractile myosin stresses in the cell interior, we initialize the bound and free myosin distributions to be $m(x, y) = b(x, y) = \sin(\pi y)^2$, such that myosin is peaked at $y = 0.5$ and drives flows away from the leading edge at $y = 1$. We utilize the same model parameters as in Fig. 7, though a range of parameters will yield similar results, and numerically simulate until the stress fibers are at steady state. Fig. S5 demonstrates that stress fibers dramatically affect lamellipodial flow at the leading edge, leading to arced flow profiles which are fastest between stress fibers and halted at the focal adhesions at the stress fiber end, matching the experimentally observed flows in Alexandrova et al. (2008). This demonstrates that our model can reproduce physiological phenomena observed in thin, spread cells where the bulk actomyosin network dynamics are effectively 2D.

References

Alexandrova, A.Y., Arnold, K., Schaub, S., Vasiliev, J.M., Meister, J.-J., Bershadsky, A.D., Verkhovsky, A.B.: Comparative Dynamics of Retrograde Actin Flow and Focal Adhesions: Formation of Nascent Adhesions Triggers Transition from Fast to Slow Flow. PLOS ONE **3**(9), 3234 (2008) https://doi.org/10.1371/journal.pone.0003234

Abraham, V.C., Krishnamurthi, V., Taylor, D.L., Lanni, F.: The actin-based nanomachine at the leading edge of migrating cells. Biophysical Journal **77**(3), 1721–1732 (1999) https://doi.org/10.1016/S0006-3495(99)77018-9

Bausch, A.R., Ziemann, F., Boulbitch, A.A., Jacobson, K., Sackmann, E.: Local measurements of viscoelastic parameters of adherent cell surfaces by magnetic bead microrheometry. Biophysical Journal **75**(4), 2038–2049 (1998) https://doi.org/10.1016/S0006-3495(98)77646-5

Colin, A., Orhant-Prioux, M., Guérin, C., Savinov, M., Cao, W., Vianay, B., Scarfone, I., Roux, A., De La Cruz, E.M., Mogilner, A., Théry, M., Blanchoin, L.: Friction patterns guide actin network contraction. Proceedings of the National Academy of Sciences **120**(39), 2300416120 (2023) https://doi.org/10.1073/pnas.2300416120

Cramer, M.S.: Numerical estimates for the bulk viscosity of ideal gases. Physics of Fluids **24**(6), 066102 (2012) https://doi.org/10.1063/1.4729611

Gittes, F., Mickey, B., Nettleton, J., Howard, J.: Flexural rigidity of microtubules and actin filaments measured from thermal fluctuations in shape. Journal of Cell Biology **120**(4), 923–934 (1993) https://doi.org/10.1083/jcb.120.4.923

Galbraith, C.G., Sheetz, M.P.: Keratocytes Pull with Similar Forces on Their Dorsal and Ventral Surfaces. Journal of Cell Biology **147**(6), 1313–1324 (1999) https://doi.org/10.1083/jcb.147.6.1313

Kassianidou, E., Brand, C.A., Schwarz, U.S., Kumar, S.: Geometry and network connectivity govern the mechanics of stress fibers. Proceedings of the National Academy of Sciences **114**(10), 2622–2627 (2017) https://doi.org/10.1073/pnas.1606649114

Kaya, M., Higuchi, H.: Nonlinear Elasticity and an 8-nm Working Stroke of Single Myosin Molecules in Myofilaments. Science **329**(5992), 686–689 (2010) https://doi.org/10.1126/science.1191484

Livne, A., Geiger, B.: The inner workings of stress fibers–from contractile machinery to focal adhesions and back. Journal of Cell Science **129**(7), 1293–1304 (2016) https://doi.org/10.1242/jcs.180927

Labouesse, C., Gabella, C., Meister, J.-J., Vianay, B., Verkhovsky, A.B.: Microsurgery-aided in-situ force probing reveals extensibility and viscoelastic properties of individual stress fibers. Scientific Reports **6**(1), 23722 (2016) https://doi.org/10.

1038/srep23722

Luo, T., Mohan, K., Srivastava, V., Ren, Y., Iglesias, P.A., Robinson, D.N.: Understanding the cooperative interaction between myosin II and actin cross-linkers mediated by actin filaments during mechanosensation. Biophysical Journal **102**(2), 238–247 (2012) https://doi.org/10.1016/j.bpj.2011.12.020

Lu, L., Oswald, S.J., Ngu, H., Yin, F.C.-P.: Mechanical Properties of Actin Stress Fibers in Living Cells. Biophysical Journal **95**(12), 6060–6071 (2008) https://doi.org/10.1529/biophysj.108.133462

Malik-Garbi, M., Ierushalmi, N., Jansen, S., Abu-Shah, E., Goode, B.L., Mogilner, A., Keren, K.: Scaling behaviour in steady-state contracting actomyosin networks. Nature physics **15**(5), 509–516 (2019) https://doi.org/10.1038/s41567-018-0413-4

Mogilner, A., Rubinstein, B.: The physics of filopodial protrusion. Biophysical Journal **89**(2), 782–795 (2005) https://doi.org/10.1529/biophysj.104.056515

Oliver, T., Dembo, M., Jacobson, K.: Separation of Propulsive and Adhesive Traction Stresses in Locomoting Keratocytes. The Journal of Cell Biology **145**(3), 589–604 (1999)

Rubinstein, B., Fournier, M.F., Jacobson, K., Verkhovsky, A.B., Mogilner, A.: Actin-Myosin Viscoelastic Flow in the Keratocyte Lamellipod. Biophysical Journal **97**(7), 1853–1863 (2009) https://doi.org/10.1016/j.bpj.2009.07.020

Riedel, L., Wössner, V., Kempf, D., Ziebert, F., Bastian, P., Schwarz, U.S.: The positioning of stress fibers in contractile cells minimizes internal mechanical stress. arXiv. arXiv:2407.07797 [cond-mat, physics:physics, q-bio] (2024). https://doi.org/10.48550/arXiv.2407.07797 . http://arxiv.org/abs/2407.07797

Ruppel, A., Wörthmüller, D., Misiak, V., Kelkar, M., Wang, I., Moreau, P., Méry, A., Révilloud, J., Charras, G., Cappello, G., Boudou, T., Schwarz, U.S., Balland, M.: Force propagation between epithelial cells depends on active coupling and mechano-structural polarization. eLife **12**, 83588 (2023) https://doi.org/10.7554/eLife.83588

Schwarz, U.S., Erdmann, T., Bischofs, I.B.: Focal adhesions as mechanosensors: The two-spring model. Biosystems **83**(2), 225–232 (2006) https://doi.org/10.1016/j.biosystems.2005.05.019

Schwarz, U.S., Safran, S.A.: Physics of adherent cells. Reviews of Modern Physics **85**(3), 1327–1381 (2013) https://doi.org/10.1103/RevModPhys.85.1327

Uehara, R., Goshima, G., Mabuchi, I., Vale, R.D., Spudich, J.A., Griffis, E.R.: Determinants of Myosin II Cortical Localization during Cytokinesis. Current Biology **20**(12), 1080–1085 (2010) https://doi.org/10.1016/j.cub.2010.04.058